Clim Dyn
DOI 10.1007/s00382-016-3166-8

Model performance metrics and process diagnostics for boreal summer intraseasonal variability

J. M. Neena[1,3] · Duane Waliser[1,2] · Xianan Jiang[1]

Received: 4 December 2015 / Accepted: 8 May 2016

Abstract Representation of the boreal summer intraseasonal oscillations (BSISO) is evaluated in the 20-year climate simulations from 27 general circulation models (GCMs), produced as part of a global multi-model evaluation project coordinated to study the vertical structure and physical processes of the Madden–Julian oscillation (MJO). Model performance metrics are developed to assess the simulated BSISO characteristics, with a special focus on its northward propagation over the Asian monsoon domain. Several process-oriented diagnostics developed by the MJO community are also tested for the BSISO. Simulating the phase speed and meridional extent of BSISO northward propagation, the northwest–southeast tilted rainband structure and the quasi-biweekly mode are identified as some of the persisting problems for many GCMs. Interestingly, many of the GCMs, which capture BSISO eastward propagation, also show good fidelity in simulating BSISO northward propagation. Meridional vertical profiles of anomalous wind, temperature and diabatic heating of BSISO are better simulated in the GCMs that simulate the northward propagation. Process-oriented diagnostics based on seasonal mean vertical shear of zonal and meridional wind, large-scale rain fraction and relative humidity are also examined, but it still remains challenge to find a process diagnostic which is strongly linked to BSISO northward propagation. The complex spatial structure and presence of multi-scale disturbances, demand the development of more focused GCM evaluation metrics and process diagnostics specifically for the BSISO.

Keywords Boreal summer intraseasonal oscillation · Process oriented diagnostic metrics · Multi-model evaluation

Electronic supplementary material The online version of this article (doi:10.1007/s00382-016-3166-8) contains supplementary material, which is available to authorized users.

✉ J. M. Neena
neena@iiserpune.ac.in; neenajm@gmail.com

[1] Joint Institute for Regional Earth System Science and Engineering, University of California, Los Angeles, CA, USA

[2] Jet Propulsion Laboratory, California Institute of Technology, Pasadena, CA, USA

[3] Indian Institute of Science Education and Research, Pune, India

1 Introduction

Intraseasonal or sub-seasonal variability (ISV) is a prominent feature of the tropical ocean–atmospheric system, which interacts with both the weather and climate scales. The different phenomena influenced by tropical ISV include, the diurnal cycle of tropical convection (Tian et al. 2006; Oh et al. 2012), tropical cyclone activity (Bessafi and Wheeler 2006), synoptic disturbances over the monsoon trough (Goswami et al. 2003; Neena and Goswami 2010), Asian and Australian monsoons (Sikka and Gadgil 1980; Hendon and Liebmann 1990; Webster et al. 1998; Goswami 2005), and the El nino southern oscillation (ENSO) (Lau and Chan 1988; Takayabu et al. 1999; McPhaden 1999). For further description, refer to the reviews in Lau and Waliser (2011). Some manifestations of ISV exhibit a quasi-oscillatory behavior, with relatively repeatable patterns of variability and propagation, and are generally referred to as tropical intraseasonal oscillations (ISOs). The Madden–Julian oscillation (MJO) is the most common and energetic of these oscillations (Madden and Julian

Published online: 14 May 2016

1972, 1994; Wheeler and Kiladis 1999; Zhang 2005; Lau and Waliser 2011). The MJO represents the planetary scale convectively coupled eastward propagating disturbance of 30–60 day periodicity, which is more active during boreal winter (Madden 1986).

Tropical ISOs show pronounced seasonality in their properties such as spatial structure, propagation, periodicity and domain of activity (Zhang and Dong 2004; Wang et al. 2006; Waliser 2006a, b; Jiang and Waliser 2008; Kikuchi et al. 2011). The seasonality of tropical ISOs is thought to be the result of changes in the mean background flow, since ISOs are fluctuations about seasonal mean state (Wang and Xie 1997). The boreal summer ISO (BSISO) typically refers to the dominant quasi-oscillatory mode that affects the Asian summer monsoon (Webster et al. 1998; Goswami 2005; Waliser 2006a, b), although there is significant summertime intraseasonal variability over the eastern Pacific as well (e.g. Maloney and Esbensen 2007; Jiang and Waliser 2009). The BSISO typically exhibits a shorter period than boreal winter MJO (Wang et al. 2006) and features a strong northward propagating component that extends its influences over the entire south Asian Monsoon domain. The different mechanisms propounded for BSISO northward propagation includes (1) Rossby wave responses to equatorial eastward propagation (Wang and Xie 1997; Kemball-Cook and Wang 2001), (2) barotropic vorticity induced by mean easterly vertical wind shear (Jiang et al. 2004), (3) air–sea interaction (Kemball-Cook and Wang 2001; Fu et al. 2003) (4) wind induced moisture-convection feedbacks (Bellon and Sobel 2008a), (5) meridional advection of baroclinic vorticity anomalies by the vertical shear of mean meridional wind (Bellon and Sobel 2008b), (6) equatorial beta-drift of low-level cyclonic vortices (Boos and Kuang 2010) and (7) momentum transport by cumulus convection (Kang et al. 2010).

While the winter MJO is largely equator bound and the propagation of convective anomalies are over the warm oceanic regions, a significant part of BSISO northward propagation occurs over land. Therefore, the processes controlling BSISO characteristics like moisture sensitivity and surface-feedbacks might be different from that for the winter MJO. Global climate models (GCM) are known to have serious problems simulating the salient features of BSISO. Major deficiencies are observed in simulating its spatial structure, northward propagation and scale-selection (Sperber et al. 2001; Kang et al. 2002; Waliser et al. 2003; Sperber and Annamalai 2008; Lin et al. 2008; Sperber et al. 2013; Sabeerali et al. 2013). The northwest–southeast tilted rain band structure is another feature that is often misrepresented in the models (Waliser et al. 2003; Sperber and Annamalai 2008; Sperber et al. 2013; Sabeerali et al. 2013). This is often associated with the models' limitations in simulating the eastward propagation and the associated wave responses (Sperber and Annamalai 2008).

Nevertheless, over the past two decades, there has been some progress in the simulation and prediction of BSISOs (Sabeerali et al. 2013; Abhilash et al. 2014). Fidelity of GCMs in simulating tropical ISOs is often taken as a test bed for assessing the performance of physical parameterization schemes. For the MJO, poor GCM performance is often attributed to the inadequacies in deep convection parameterization (Wang and Schlesinger 1999; Maloney and Hartmann 2001; Lin et al. 2006; Zhang and Song 2009; Zhou et al. 2012). Concentrated effort towards improving MJO simulation has resulted in better identification of the malfunctioning parts of model physics and its rectification (Benedict and Randall 2007; Waliser et al. 2009; Bechtold et al. 2008; Kim et al. 2011, 2014; Jiang et al. 2015). Although some of the diagnostic tools made for the MJO might also be applied to the BSISOs, its much more complex spatial structure and the presence of multi-scale disturbances demand the development of more focused GCM evaluation metrics. Our understanding of the model deficiencies causing the poor simulation of BSISO northward propagation is still limited, and it calls for exploring more process-oriented diagnostic tools exclusively for the BSISO. Additionally, due to the large-scale influences of BSISO on the strength and variability of the Asian summer monsoon, such process diagnostics would also prove to be valuable for simulating and predicting the monsoon.

In this study we make an attempt to better understand the BSISO and identify the key processes behind the good versus poor performance of the GCMs in simulating the mode, by developing and applying a set of GCM evaluation metrics and diagnostics. The BSISO evaluation is carried out using the multi-model simulations from the year of Tropical convection (YOTC) MJO task force (MJOTF) and GEWEX global atmospheric system study (GASS) MJO vertical structure and physical processes experiment (Petch et al. 2011), following the study by Jiang et al. (2015) which focused on the simulation of boreal winter MJO. The manuscript is organized as follows. Section 2 provides descriptions of participating GCMs, details of model experiment design and the YOTC/MJOTF-GASS project objectives. Section 3 presents the details of the performance evaluation of BSISOs in participating GCMs and process-oriented metrics developed for BSISOs. Main results and insights obtained from this study are summarized in Sect. 4.

2 Participating models and observational data sets

The YOTC/MJOTF-GASS MJO global multi-model comparison project consists of three experiments, namely, 20-year climate simulations, 2-day hindcasts, and 20-day hindcasts. One main motivation for this experimental design was to understand the linkages between model biases in long-term climate simulations and short-range forecasts (Phillips et al. 2004). Please refer to Petch et al. (2011) and the project website[1] for further details on the experiments. The vertical structure and diabatic processes of the boreal winter MJO in the 20-year climate simulations were studied by Jiang et al. (2015), and model skill for the MJO in 2 and 20-day hindcasts were reported by Xavier et al. (2015) and Klingaman et al. (2015a, b), respectively. The present study is a counterpart to Jiang et al. (2015) but with a focus on the BSISO in the climate simulation component of the experiment.

A list of models participating in the 20-year climate simulation experiment, along with the original horizontal and vertical resolutions of each model, is given in Table 1 in Jiang et al. (2015). The model output is archived at a common horizontal (2.5° × 2.5°) resolution with 22 vertical pressure levels, and 6-h temporal resolution. Of the 27 GCM simulations evaluated in this study, 22 are from atmospheric-only GCM (AGCM) runs and five are from atmosphere–ocean coupled GCM (CGCM) runs. The AGCM runs were forced using weekly NOAA Optimum Interpolation V2 sea surface temperatures (SST) and sea ice boundary conditions (Reynolds et al. 2002) from 1991 to 2010. The CNRM model runs provide a unique opportunity to understand the benefit of interactive atmosphere–ocean coupling for simulating the BSISO. Both AGCM and CGCM runs are available based on the same AGCM (CNRM-AM and CNRM-CM). In addition, the CNRM model also produced an AGCM run forced by monthly mean SST boundary conditions from the coupled run (CNRM-ACM). Additionally, SPCAM3 and SPCCSM3 are atmosphere-only and coupled runs based on the same AGCM ("super-parameterized" Community Atmospheric model Version 3 (CAM3) but with the "super-parameterization" approach in place of conventional cumulus parameterization (Randall et al. 2003; Khairoutdinov et al. 2008; Stan et al. 2010.

To evaluate model simulations, we mainly used wind, temperature, specific humidity, and vertical velocity fields from ERA-interim reanalysis (Dee et al. 2011) and TRMM-3B42 v7 rainfall (Huffman et al. 1995) for the period from 1998 to 2012. All fields were interpolated onto the same 2.5° × 2.5° grid used for the GCM output.

3 Results and discussion

3.1 Summer mean and variance

The main focus of the present study is to evaluate how well the BSISO, particularly its northward propagation, is simulated by the GCMs, and to develop a set of metrics to compare and quantify the performance of GCMs. We consider the May–October period as representing the boreal summer season, and all the analyses are performed for this season. The summer mean (May–October) precipitation and 850 hPa winds simulated by the 27 models are shown in Fig. 1, along with the observed counterpart (top left panel). The 15°S–30°N, 50°–150°E region shown in the maps defines the BSISO domain for this study. Significant biases are observed in the model simulations of summer mean precipitation, particularly over land region. While the models exhibit varying degrees of fidelity in simulating the different locations of precipitation maxima over the Asian monsoon domain, some notable biases are the overestimation of precipitation over the western–north Pacific (WNP) (e.g. MRI-AGCM3, BCC-AGCM2.1, GISS-E2, SPCAM3) and the southwest equatorial Indian Ocean (EQIO) (e.g. FGOALS-s2, CWB-GFS, CFS2, BCC-AGCM2.1). These systematic biases might be related to the models excessive response to local SST gradient (Bollasina and Ming 2013). Underestimation of summer mean precipitation over Indian land region is also noted in many models (e.g., ACCESS1, NavGEM1, BCC-AGCM2.1, CNRM-CM, CNRM-ACM). The precipitation biases appear to be linked to the 850 hPa mean wind biases as reported by Sperber et al. (2013). For example, the elongated precipitation band extending from 60° to 150°E simulated by GISS-E2, SPCAM3 and MRI-AGCM3 are associated with an eastward extending band of westerlies. Pattern correlation values were computed between the model simulated summer mean precipitation patterns and the observed precipitation pattern.

BSISO amplitude is estimated from the standard deviation (SD) of 20–90 day filtered precipitation (Fig. 2). The observed and GCM simulated precipitation are first subject to a pre-processing step involving removal of climatological annual cycle (annual mean plus first three harmonics), before the 20–90 day band-pass filter is applied. Pattern correlation values were computed between the model simulated and observed BSISO SD patterns. As evident from Figs. 1 and 2, in most models, the dominant features in BSISO SD patterns closely follow the summer mean patterns, in agreement with many previous studies (e.g. Sperber et al. 2000; Goswami and Ajaya Mohan 2001; Waliser et al. 2003). The pattern correlation values for summer mean precipitation for the 27 models show a high correlation with the pattern correlation values for BSISO SD (correlation coefficient r = 0.82, not shown). A correlation coefficient of 0.32 is significant at the 95 % level based on a one-tailed Student's *t* test. Over the Bay of Bengal (BoB), WNP, Western Ghats and the eastern EQIO, variance in the 20–90-day timescale is underestimated to a large degree in many models. The coefficient of variance (defined as the standard deviation normalized by

[1] https://www.earthsystemcog.org/projects/gass-yotc-mip/.

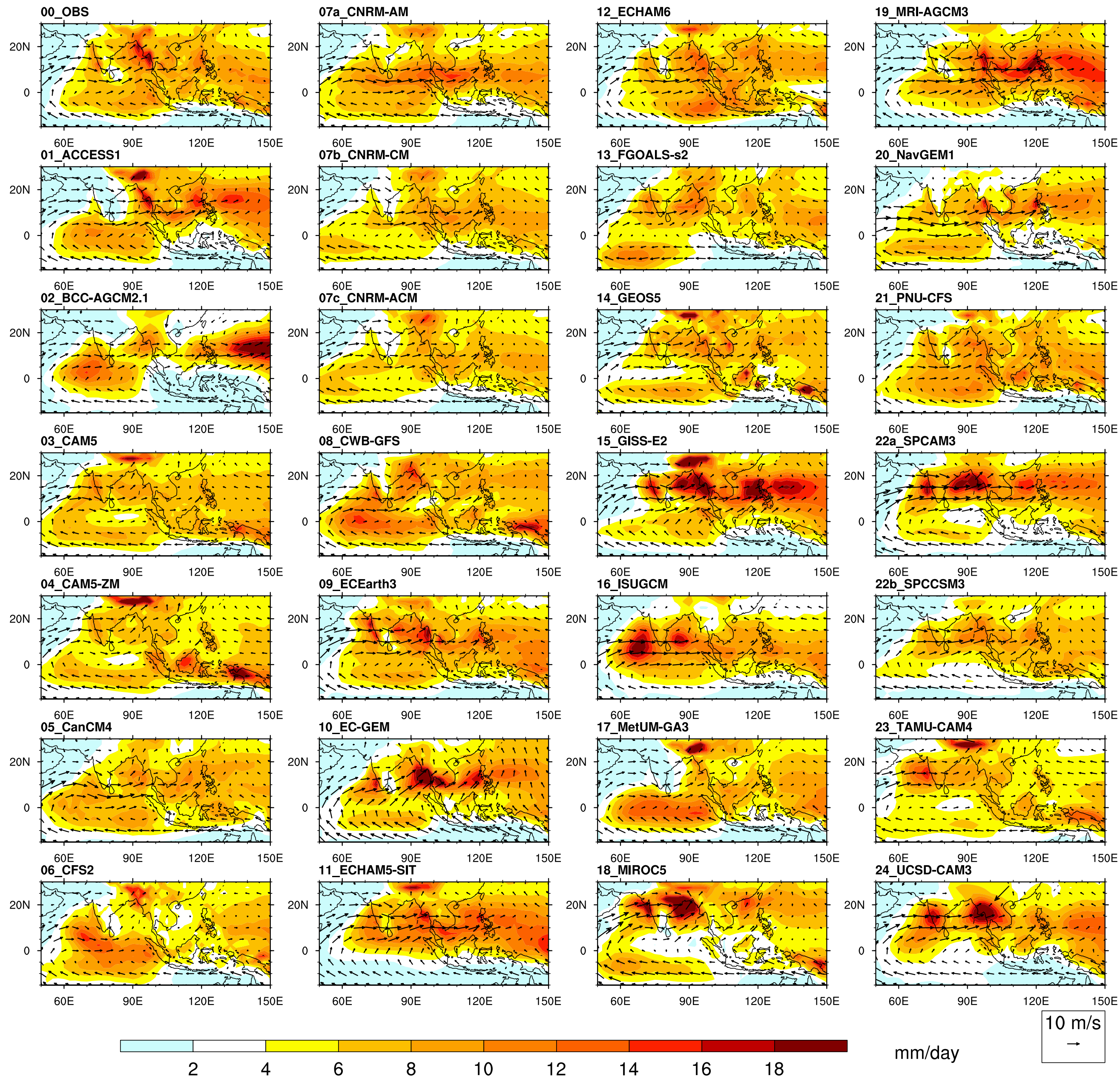

Fig. 1 Summer mean May–October) rainfall (*shaded*, mm/day) and winds at 850 hPa (vectors, m s^{-1}) in observations (TRMM and ERA-interim, 1998–2012) and multi-model simulations (1991–2010)

the mean) was also computed to see if the observed biases in BSISO SD were solely determined by the summer mean state biases (not shown). But the regions of large biases in BSISO SD also exhibited high coefficient of variance indicating that the BSISO amplitude biases are not totally determined by the mean state biases. ECEarth3, PNU-CFS, GISS-E2, ACCESS1 and ECHAM6 are some of the models that show better skill in simulating BSISO variance pattern.

The multi-model average of summer mean precipitation is shown in Fig. 3a. The most pervasive systematic biases across the models are highlighted by the multi-model mean bias and centered RMSE maps shown in Fig. 3b, c. Mean bias is computed as the difference between multi-model mean and observation. Then, across the 27 models, the centered RMSE is computed with respect to observation after removing the multi-model mean bias from each of the model simulation. Particularly notable are the underestimation of summer

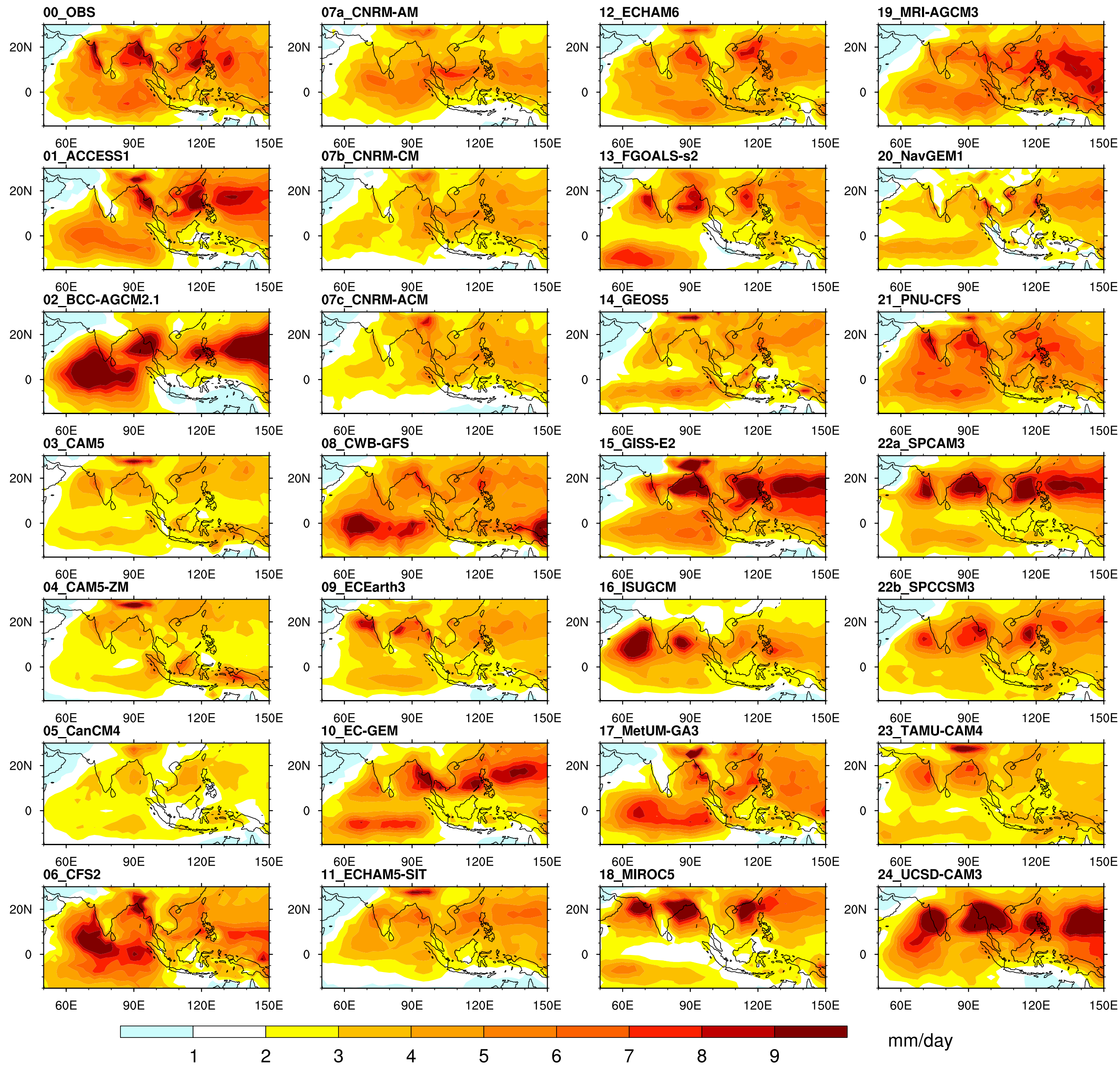

Fig. 2 Standard deviation of daily 20–90 day band-pass-filtered rainfall anomalies during boreal summer (May–October) based on observations and model simulations (unit: mm day $^{-1}$)

precipitation over BoB, the eastern EQIO and most part of South Asian land mass and the overestimation of seasonal mean precipitation over Arabian Sea, western Indian Ocean (IO) and WNP (Fig. 3b) and the overall large errors (of either sign) over IO and WP regions (Fig. 3c). Similar to Fig. 3a–c, the multi-model average intraseasonal precipitation SD, its bias and RMSE are shown in Fig. 3d–f. Multi-model average intraseasonal amplitude is marked by negative biases over BoB, northwest India, eastern EQIO and WP (Fig. 3e) and large RMSE over Arabian sea, western EQIO, western Indochina peninsula, eastern Himalayas, and WNP (Fig. 3f).

3.2 BSISO life cycle

Following the examination of GCM skill in capturing the spatial distribution of BSISO amplitude, we now examine the model fidelity in representing spatial patterns associated with different phases of BSISO, i.e., the BSISO life cycle. The observed BSISO life cycle is brought out through an extended empirical orthogonal function (EEOF) analysis of longitudinally averaged (60°–95°E) TRMM 3B42 precipitation anomalies (unfiltered, only climatological annual cycle removed) over the region of 12.5°S–27.5°N,

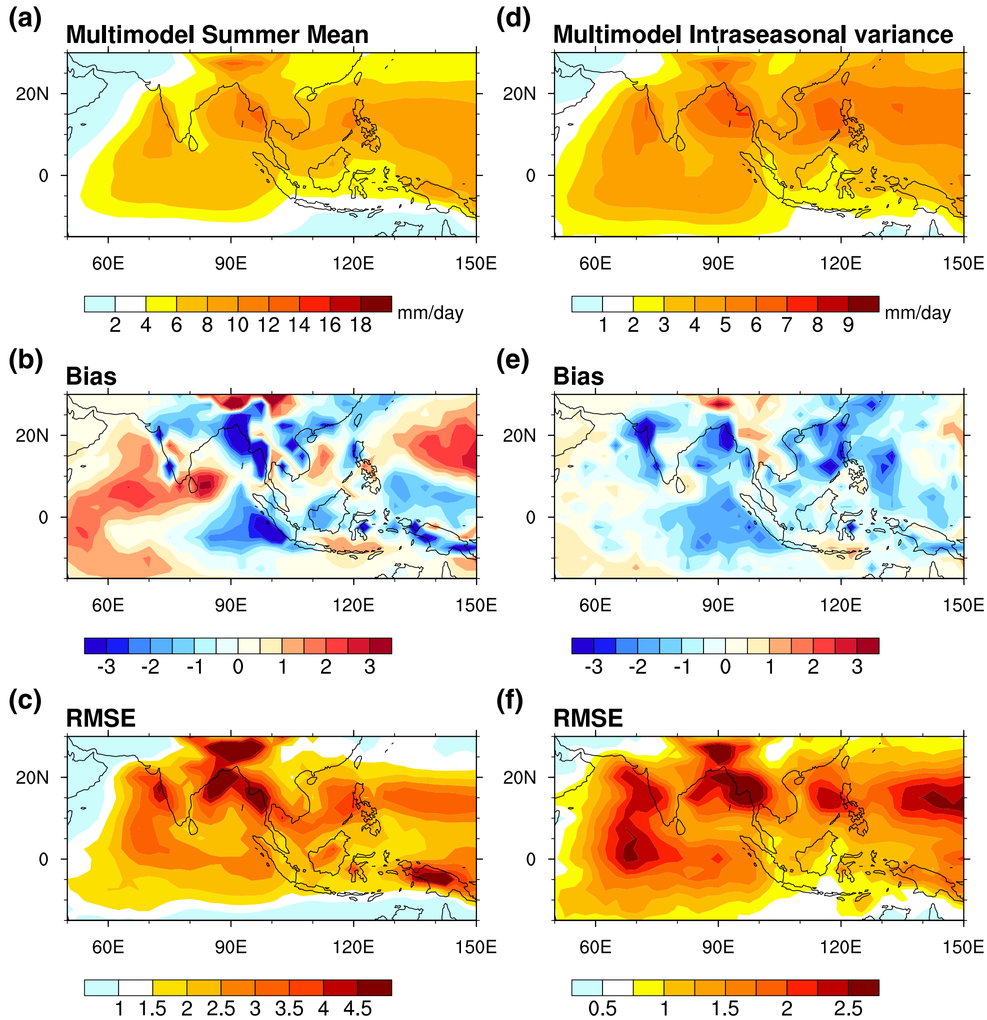

Fig. 3 **a–c** Multi-model average (27 models) of summer mean precipitation, its bias and root mean square error w.r.t. observation. **d–f** Multi-model averaged intraseasonal variance, its bias and RMSE w.r.t. observation

with 15 lags at 1-day interval (Suhas et al. 2013). The two leading EEOF modes together explain more than 23 % of variance and eight phases of BSISO can be constructed from the two leading principal components (PCs). Composites of 20–90 day filtered precipitation for the eight BSISO phases are shown in Fig. 4a. Model simulated precipitation anomalies are projected onto the observed EEOF modes to obtain the model PCs. Using these PCs as the reference time series, model BSISO phase composites are constructed (Sperber and Annamalai 2008; Sperber et al. 2013). For each BSISO phase, pattern correlations are estimated between the observed and simulated phase composites over the domain 15°S–30°N, 50°–150°E and the BSISO life cycle skill score is obtained as the average pattern correlation over the 8 phases. It exhibits a good correlation ($r = 0.62$) with the pattern correlations scores for the BSISO SD pattern (Fig. 4b), in agreement with earlier studies (Sperber et al. 2013), indicating that the large-scale structure and strength of filtered precipitation variance are largely determined by the propagating BSISO. Model fidelity for BSISO life cycle was also compared with the relative amplitudes of BSISO in the 27 models—which is defined as the domain average value of model simulated BSISO SD normalized by the corresponding value in observations (Fig. 4c). But, no significant relationship was found between the two metrics.

3.3 Propagation features

The propagation characteristics of BSISO are more complex than the winter MJO. In addition to the eastward propagating convective signals along the equator, during boreal summer the intraseasonal convective anomalies also exhibit northward propagation over the Asian monsoon domain (Sikka and Gadgil 1980; Webster et al. 1998; Jiang et al. 2004). Westward propagating convective anomalies

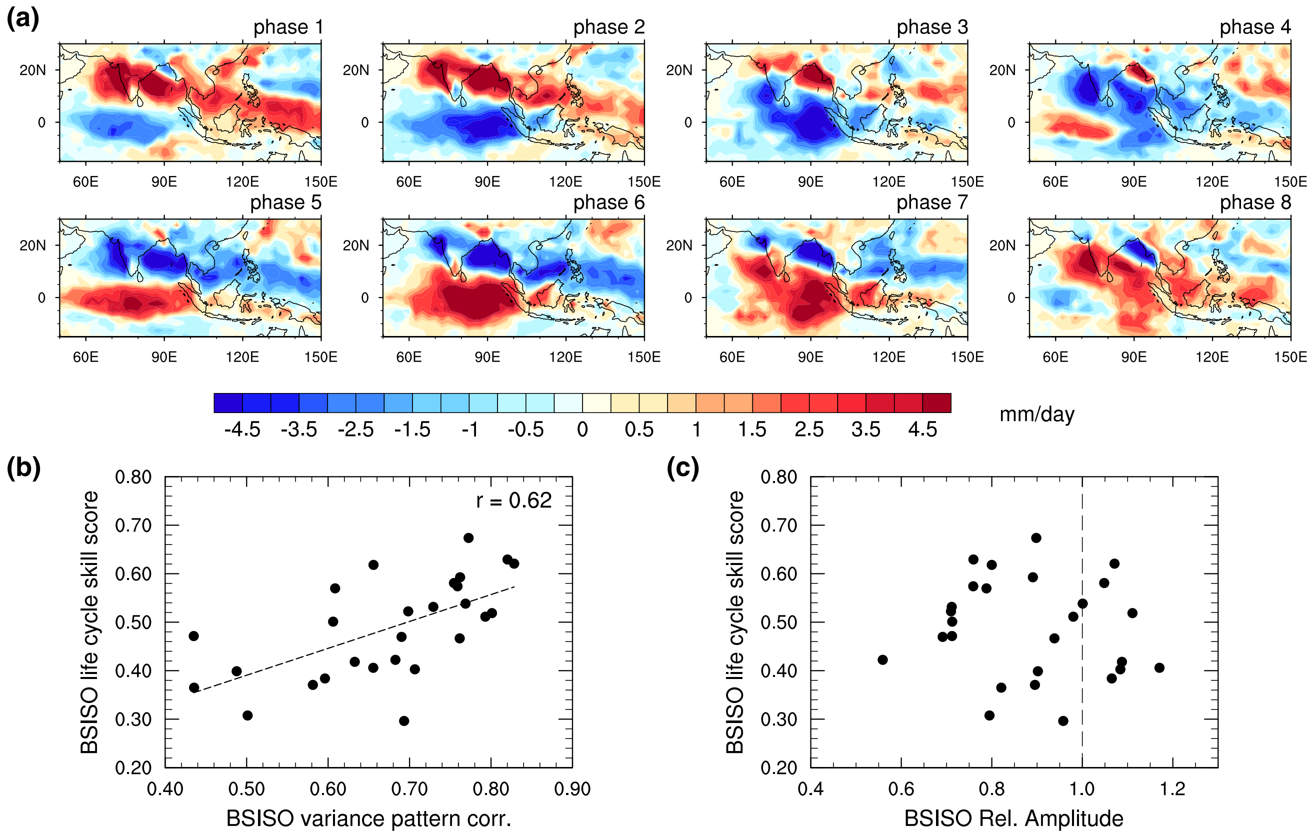

Fig. 4 **a** BSISO life cycle in TRMM rainfall. 20–90 day filtered rainfall composited for the eight BSISO phases identified through EEOF analysis. **b** BSISO life cycle scores (average pattern correlation across the eight phases for the observed and simulated BSISO life cycle) plotted against the pattern correlations for the SD patterns. **c** BSISO life cycle scores plotted against the relative amplitude of the SD patterns

associated with the quasi-biweekly (10–20 day) mode (QBM) are also characteristic of the region (Chatterjee and Goswami 2004; Kikuchi and Wang 2009). Fidelity of the models in simulating these propagation features is explored using lag-regression analysis. Regression analysis is carried out using band-pass filtered rainfall anomalies during the May–October summer season against a time series of area averaged anomalies over a suitable location, with the coefficients normalized for one standard deviation value of the base time series.

For estimating the fidelity with respect to eastward propagation of BSISO, 20–90 day filtered rainfall was regressed against the filtered rainfall anomalies averaged over an EQIO box (75°–85°E; 5°S–5°N) and a western Pacific (WP) (140°–150°E; 5°S–5°N) box, respectively, for time lags from day −20 to day +20. The lag-longitude sections of the regression coefficients were computed over longitudes 30°E–150°W by averaging the coefficients in the 10°S–10°N latitudinal band. The regression plots with respect to the EQIO reference box are shown in Fig. 5 and the regression plots with respect to the WP reference box are shown in Fig. S1. The eastward propagation phase speed of 5 ms^{-1} observed in TRMM precipitation (top left plot) is overlaid as a dashed line on all plots for comparison. The observed eastward propagating rainfall signals are reasonably simulated in a limited number of GCMs, including ECEarth3, PNU-CFS, SPCAM3, GISS-E2 and MRI-AGCM3. Models like ECHAM6, CNRM-CM, CNRM-ACM, CAM5-ZM, ECHAM5-SIT, and ACCESS1 show some skill over the Indian Ocean, but fail to simulate the propagation of convective anomalies across the Maritime Continent. Pattern correlations were estimated between the observed and simulated lag-regression patterns. The skill scores for BSISO eastward propagation were estimated as the average of the two pattern correlation scores obtained from Fig. 5 and Fig. S1. Jiang et al. (2015) evaluated the winter MJO eastward propagation skill for the same set of models using the same approach.

The most dominant feature of the BSISO is its northward propagation. We examine the performance of the models in capturing the BSISO northward propagation using a similar lag-regression based approach. 20–90 day filtered rainfall was regressed with respect to the area averaged filtered rainfall anomalies over a near equatorial box (85°–90°E;

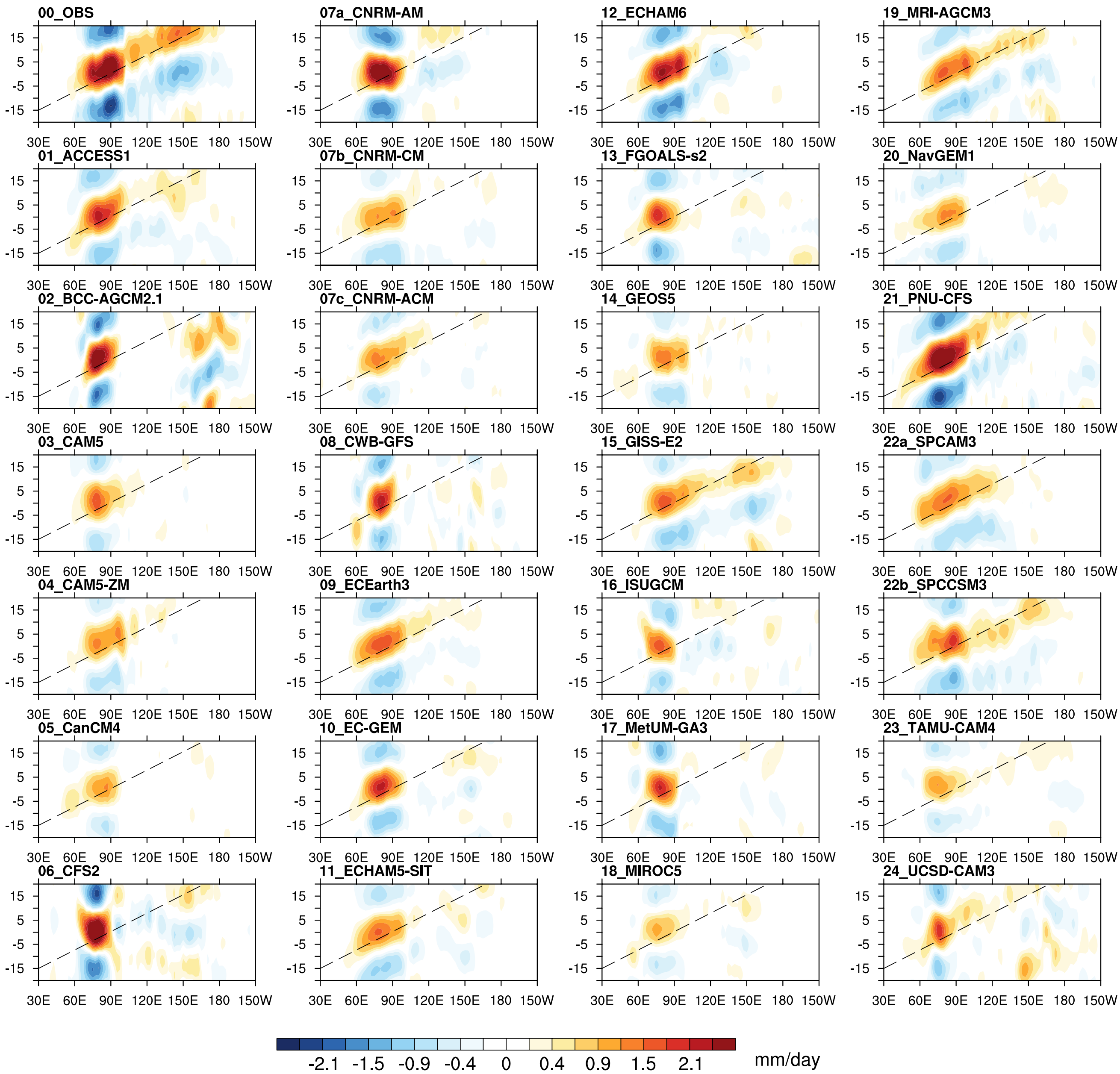

Fig. 5 Longitude-time evolution of 20–90 day band-pass-filtered rainfall anomalies regressed against itself averaged over an eastern equatorial Indian Ocean box (75°–85°E; 5°S–5°N). Regressed anomalies are averaged over 10°S–10°N. *Dashed lines* in each panel denote the 5 m s^{-1} eastward propagation phase speed

5°–10°N) and also an off equatorial box (85°–90°E; 15°–20°N), for time lags from day −20 to +20. The time-latitude Hovmöller diagrams of regressed anomalies (averaged over 80°–100°E longitudes) with respect to the two base points are shown in Fig. 6 and Fig. S2 respectively. The northward propagation speed for BSISO in observations is ~1° latitude per day (indicated by the dashed line in each panel). The skill scores for BSISO northward propagation were estimated as the average of the two pattern correlation scores obtained from Fig. 6 and Fig. S2. For the remainder of the manuscript, this pattern correlation based metric is used as the primary measure for model fidelity for BSISO northward propagation. PNU-CFS, ECHAM6, ECEarth3, GEOS5 and SPCCSM3 are some models that show superior skill in simulating BSISO northward propagation.

In addition to the northward and eastward propagating mode, a 10–20 day quasi-biweekly mode (QBM) is also a dominant feature observed over the south/south-east Asian sector during boreal summer (Chatterjee and Goswami 2004). The QBM is westward propagating and is known

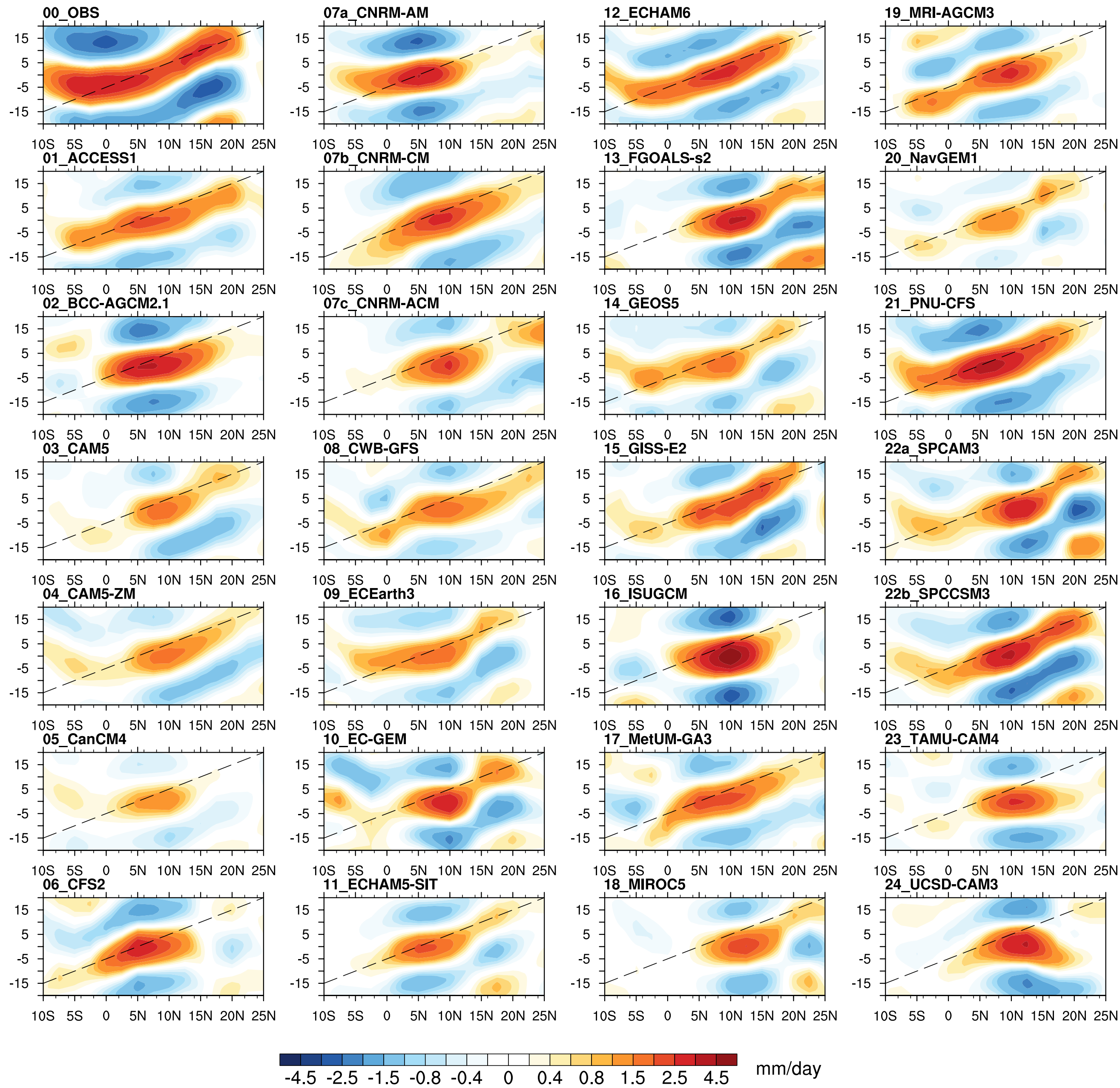

Fig. 6 Latitude-time evolution of 20–90 day band-pass-filtered rainfall anomalies regressed against itself averaged over a near equatorial box (85°–90°E; 5°–10°N). Regressed anomalies are averaged over 80°–100°E. *Dashed lines* in each panel denote the 1° latitude day^{-1} northward propagation phase speed

to interact with the northward and eastward propagating BSISO. To bring out the westward propagation associated with the QBM, 10–20 day filtered rainfall was regressed with respect to the area averaged filtered rainfall anomalies over the Bay of Bengal (BOB) (85°–90°E; 10°–15°N), for time lags from day −10 to +10. The time-longitude sections of the regression coefficients (Fig. 7) were computed by averaging the coefficients in the 10°–15°N latitudinal band. The observed phase speed for westward propagation from WP to the IO is about 6 ms^{-1} and is denoted by the dashed line in each panel. Many models have difficulty in representing the QBM westward propagation extending from the WP to the IO longitudes. In some models, the mode appears localized over the IO sector, while other models fail to capture the difference in propagation characteristics over the WP and IO. ECHAM6, SPCAM3,

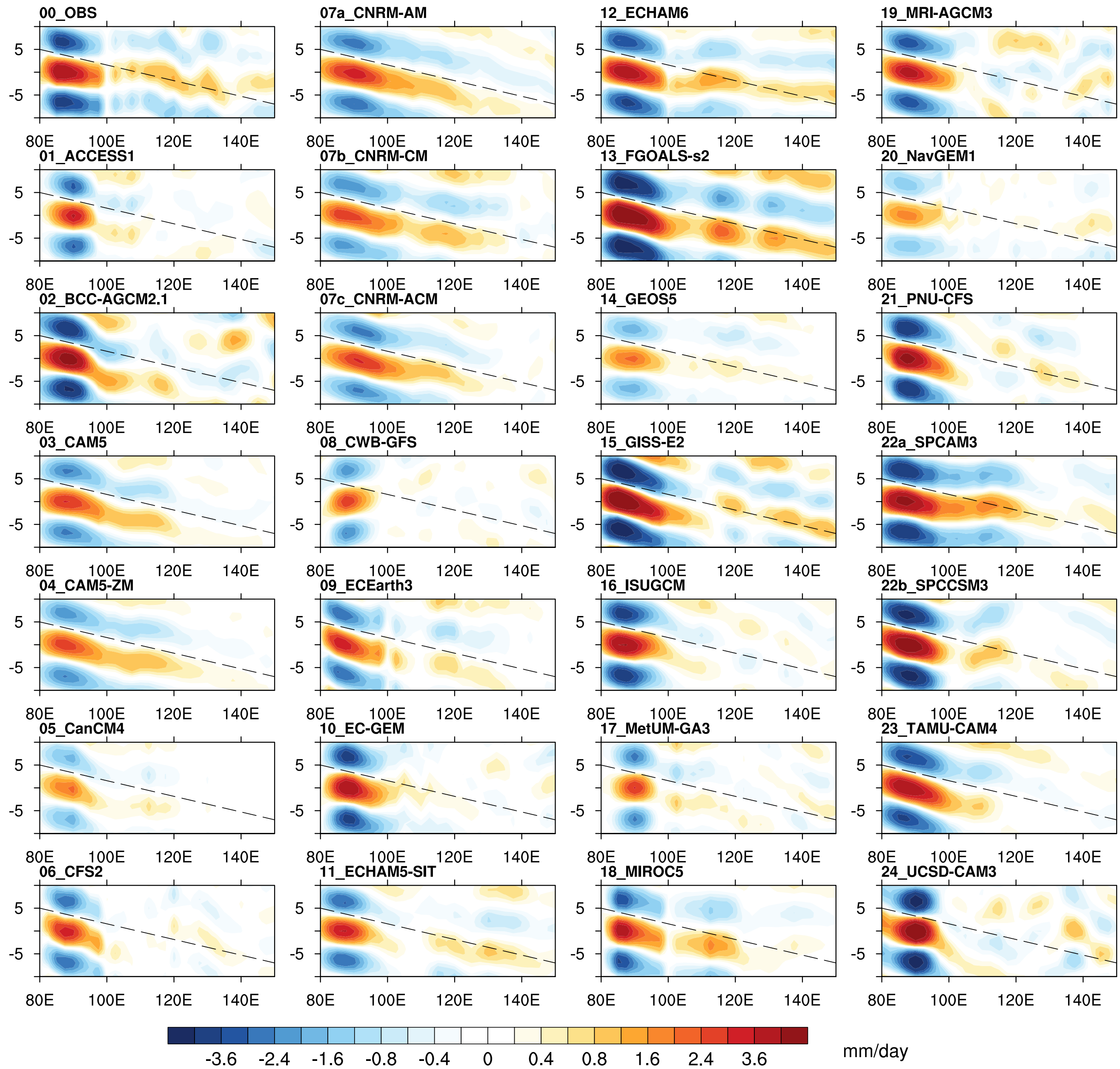

Fig. 7 Longitude-time evolution of 10–20 day band-pass-filtered rainfall anomalies regressed against itself averaged over a Bay of Bengal (BOB) box (85°–90°E; 10°–15°N). Regressed anomalies are averaged over 10°–15°N. *Dashed lines* in each panel denote the 6 m s^{-1} westward propagation phase speed

SPCCSM3, EC-GEM, PNU-CFS and GEOS5 are some models that simulate the westward propagation of QBM with good fidelity.

In Fig. 8a–c we compare and contrast the model skill scores for eastward and northward propagation of the BSISO and westward propagation of the QBM. Figure 8a compares the BSISO eastward propagation skill scores with the winter MJO eastward propagation skill scores computed by Jiang et al. (2015). A correlation of 0.6 is observed between the two skill scores. For some models, some seasonal differences are observed in the skill for simulating the MJO. For example, CNRM-CM, ECHAM5-SIT show relatively better skill in simulating the winter MJO than the summer counterpart, while some models like EC-GEM and NavGEM1 exhibit relatively higher skill in simulating the summer MJO. In Fig. 8b, the skill scores for BSISO northward propagation is compared with the BSISO eastward propagation skill scores. One of the theories for BSISO northward propagation suggests that it arises from Rossby wave responses to BSISO eastward

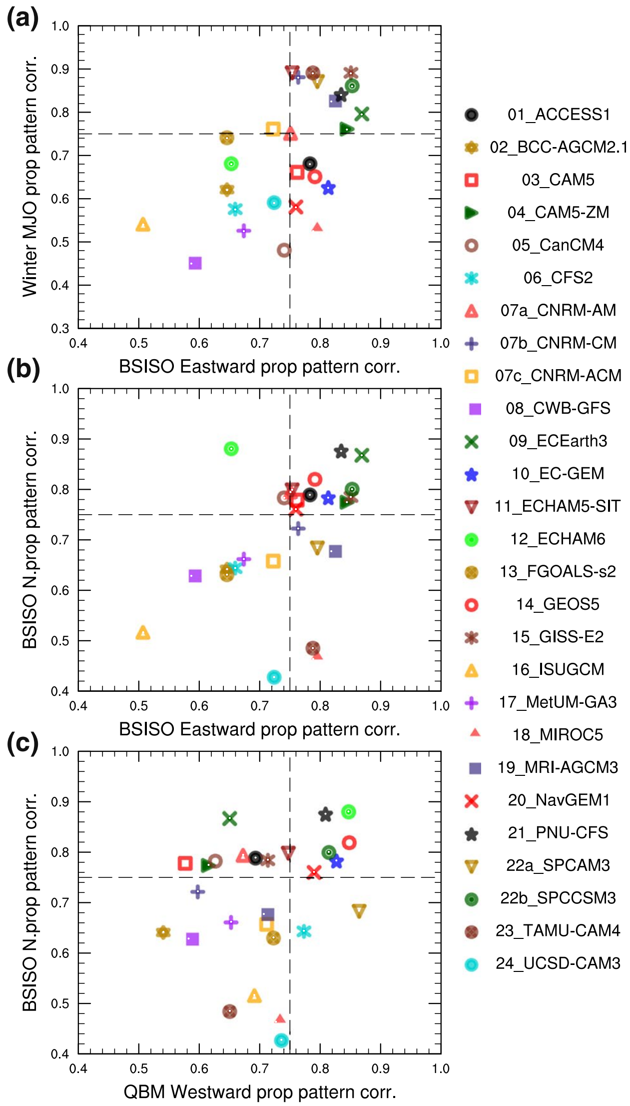

Fig. 8 **a** Skill scores for BSISO eastward propagation plotted against wintertime MJO eastward propagation scores (r = 0.6). **b** Skill scores for BSISO northward propagation plotted against BSISO eastward propagation scores (r = 0.44). **c** Skill scores for BSISO northward propagation plotted against QBM westward propagation scores (r = 0.22)

propagation (Wang and Xie 1997; Lawrence and Webster 2002). Sperber and Annamalai (2008) showed that the models that are skillful in simulating poleward propagation of BSISO also simulate the eastward propagation with good fidelity. Consistent with Sperber and Annamalai (2008), a large number of models with high scores for northward propagation also show better skill in simulating the eastward propagation. ECHAM6 is an exception, which exhibits good skill for the northward propagation but relatively poor skill for eastward propagation. UCSD-CAM4, MIROC5 and TAMU-CAM4 exhibit moderate to good skill in simulating BSISO eastward propagation, but the northward propagation component is not well represented. TAMU-CAM4, for which the observed MJO heating structure was incorporated into the CAM4 model design (Lappen and Schumacher 2012), is an interesting case: it shows good fidelity in simulating the equatorial MJO, but not the poleward-propagating component. These four models indicate that, simulating the eastward propagation may not be a necessary and sufficient condition for simulating the northward propagation and vice versa. The correlation between BSISO eastward and northward propagation skill scores is 0.44 and excluding the above-mentioned four models the correlation is 0.71 (Fig. 8b). The model skill in simulating BSISO northward propagation is contrasted against the skill for simulating the QBM westward propagation in Fig. 8c. No significant relationship is observed (r = 0.22).

3.4 Summarizing portrait diagram

Figure 9 presents the above discussed model evaluation metrics in the form of a "portrait diagram" (e.g. Gleckler et al. 2008), which readily summarizes the pattern correlation scores of the 27 models. Pattern correlation values for simulated summer mean precipitation pattern (Fig. 1), seasonal mean wind pattern (sum of pattern correlations for zonal and meridional wind patterns, Fig. 1), BSISO rainfall SD (Fig. 2), BSISO U850 SD (figure not shown), BSISO northward propagation in precipitation (Fig. 6) and U850 (figure not shown), BSISO eastward propagation in precipitation (Fig. 5) and QBM westward propagation (Fig. 7) are given in the summarizing portrait diagram. (To evaluate the northward propagation of BSISO in 850 hPa zonal wind, 20–90 day filtered U850 anomalies were regressed an area averaged index of 20–90 day filtered anomalies over a BOB box (10°–15°N, 85°–90°E) from day −20 to +20. The standardized regression coefficients were then averaged between longitudes 80°–100°E).

3.5 Impact of air–sea coupling

The availability of three simulations of the CNRM model with different levels of air–sea coupling provides an opportunity to explore how important air–sea coupling is for BSISO. Based on the same model simulations Jiang et al. (2015) had reported that air–sea coupling improves the simulation of winter MJO eastward propagation. While MJO eastward propagation was almost absent in the AGCM run (CNRM-AM), CNRM-ACM simulated weak MJO, and the fully coupled model CNRM-CM exhibited the strongest MJO propagation. But, examining the skill scores for the coupled and uncoupled runs of the CNRM (CNRM-AM, CNRM-CM and CNRM-ACM) and the super-parameterized models (SPCAM3 and SPCCSM3) (Fig. 9), a clear conclusion could not be made regarding the effect of atmosphere–ocean

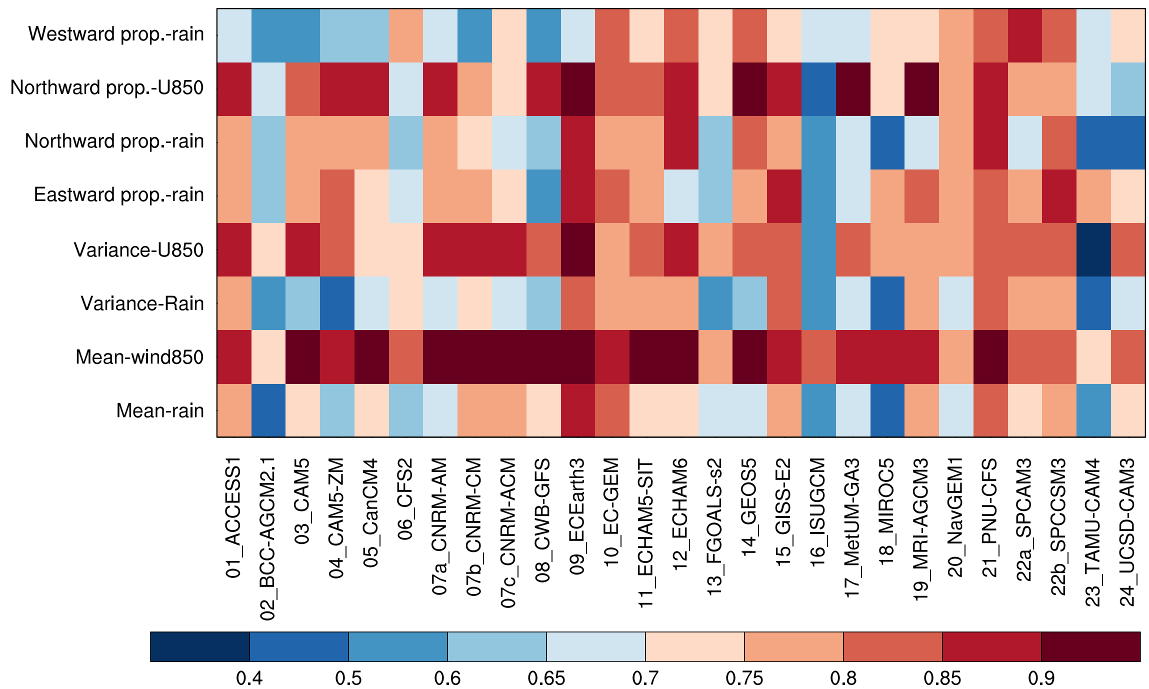

Fig. 9 Summarizing portrait diagram. Pattern correlation based skill scores of the 27 GCMs measuring their fidelity in representing the summer mean and variance and propagation characteristics of BSISO

coupling in simulating BSISO propagation. The skill for BSISO eastward and northward propagation is as good or even better for the atmosphere-only CNRM run (CNRM-AM) than the coupled run (CNRM-CM). The main difference between the AGCM and CGCM simulations arises from how the biases in the mean state of the coupled model influences the air–sea feedbacks (Klingaman and Woolnough 2014). As no marked improvement is observed in the simulation of BSISO northward propagation by the CNRM-CM it may be assumed that the boreal summer mean state biases may be inhibiting the ISV. On the other hand, between CNRM-ACM and CNRM-CM with the same mean SST, CNRM-ACM performs much poorly (Fig. 9). This difference indicates that the intra-seasonal SST variability (which gets diluted in the boundary forcing for CNRM-ACM since monthly mean SST is used), and associated air–sea feedbacks may be crucial for BSISO northward propagation. The SPCCSM3 performs slightly better than the uncoupled SPCAM3 in capturing BSISO eastward and northward propagation (Fig. 9), in agreement with results by DeMott et al. (2013).

3.6 Tilted rain band structure

One noted limitation in many GCMs associated with BSISO, is their failure to simulate the northwest–southeastward (NW–SE) tilted rain band structure (Waliser et al. 2003; Sperber and Annamalai 2008; Sperber et al. 2013; Sabeerali et al. 2013). It is well known that when similar phases of convection are found to persist over the Indian land mass and the Maritime continent and the equatorial WP, opposite phase of convective anomalies resides over EQIO and NWP giving rise to a tilted band of convection (Annamalai and Slingo 2001; Annamalai and Sperber 2005). The tilted rain-band structure is considered to arise from the Rossby wave responses associated with BSISO eastward propagation (Sperber and Annamalai 2008; Annamalai and Sperber 2005). In Fig. 10, representations of tilted rainband structure in the model simulations are examined using the lag-0 regressed rainfall anomalous pattern with respect to the off equatorial box (85°–90°E; 15°–20°N). To objectively quantify the tilt of the rainband, the regression coefficient at each grid point was first normalized by the maximum positive value in the domain 5°S–30°N, 70°–120°E. For each longitude, the latitude of maximum normalized regression coefficients was first identified, and then a least square fit was generated for these lat-lon pairs (Fig. 11a). In order to give weight to the regression coefficients amplitude, normalized regression values less than 0.1 were not considered. The NW–SE slope of the least squares fit line gives a good measure of the tilt of the convective rain-band, and a tilt of 0.3 is found in TRMM rainfall anomalies (Fig. 11a). Note that a positive tilt value means NW–SE tilt, while a negative value denotes rain belt tilt in a southwest–northeastward direction. The observed tilt (solid line) and simulated tilt (dashed line) is overlaid on the lag-zero regression plots in Fig. 10. Most models

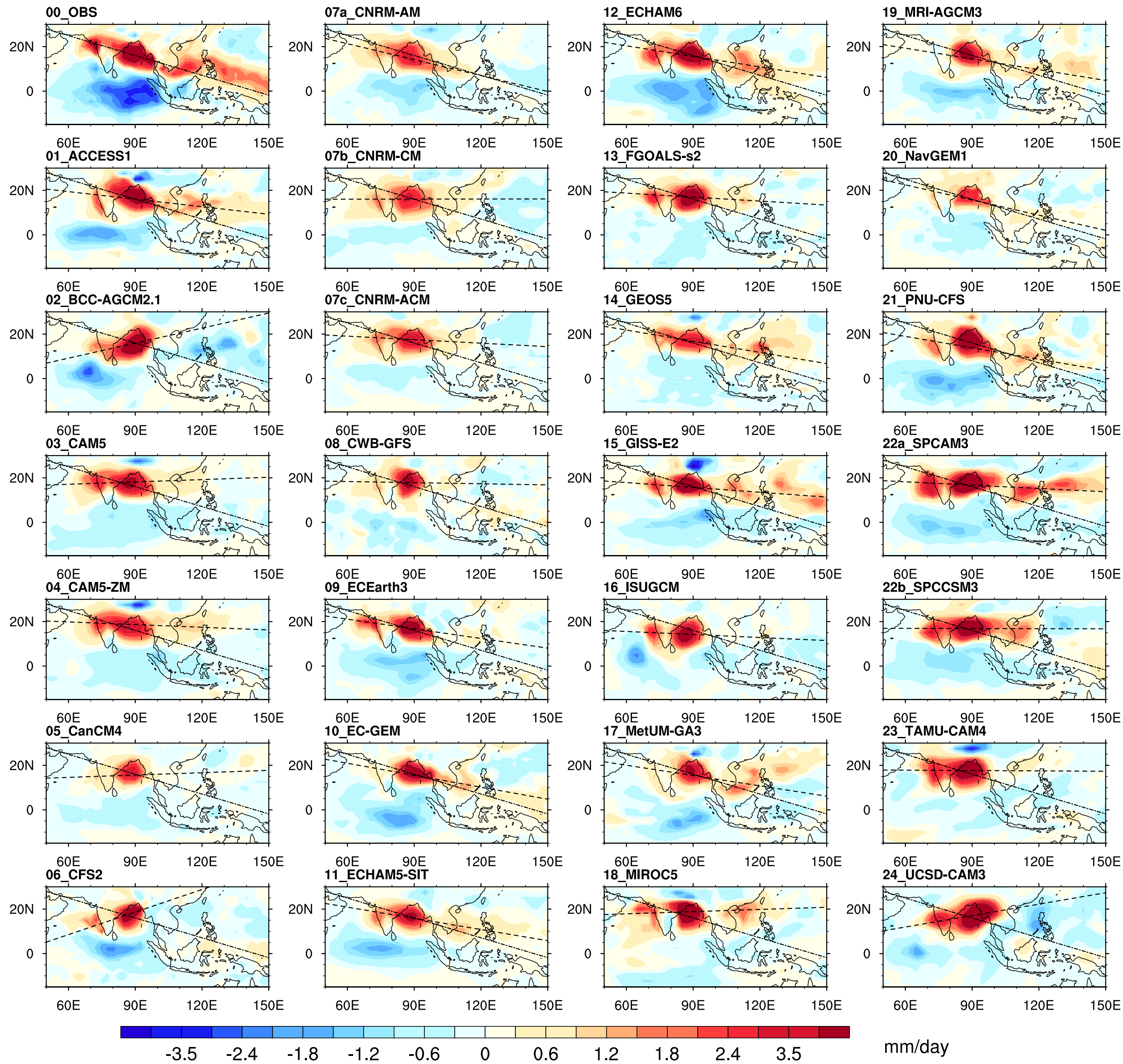

Fig. 10 Lag zero regressed anomalies of 20–90 day band-pass-filtered rainfall anomalies regressed against itself averaged over an off-equatorial box (85°–90°E; 15°–20°N). The *solid* and *dashed lines* corresponds to the slopes of the observed and simulated rain-bands. The slopes were objectively computed from the regression map

(at least two-third) capture the NW–SE tilt but with values less than 0.1, much weaker than the observed tilt of 0.3 (Fig. 10b). ECHAM6, EC-GEM, NavGEM1, CNRM-AM, and ECHAM5-SIT are several models that best represent the observed tilted rain structure of the BSISO. A good correlation (r = 0.52) is noted between the model fidelity in simulating the NW–SE tilt and northward propagation skill (Fig. 11b). Top one-third of the models with largest skill score for northward propagation are classified as "good models" (shown in red) and bottom one-third of the 27 models with lowest skill score for northward propagation are classified as "poor models" (shown in blue) and the one third which has intermediate skill are classified as "moderate models" (shown in black). In the remainder of the text this classification is followed.

3.7 Meridional-vertical structure

Next, we explore differences in the meridional-vertical structure associated with the BSISO, in models that have

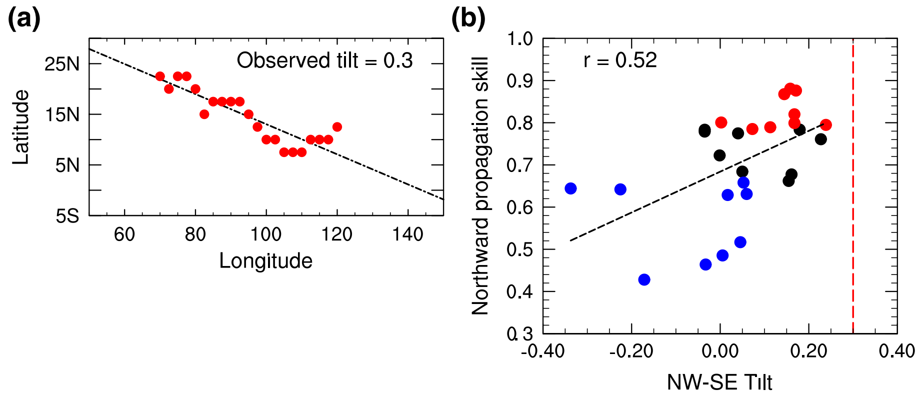

Fig. 11 **a** Computing the slope of the convective rain-band in observations. Scatter plot and least squares fit for the convection maxima points between 70° and 120°E in the lag zero regression plot (Fig. 10, *top left panel*). NW–SE tilt is taken as—slope of the regression line. **b** The simulated Northwest–Southeast (NW–SE) tilt in different models plotted against their skill in simulating BSISO northward propagation. *Red* and *blue dots* represent models with good versus poor skill for BSISO northward propagation. The observed tilt from **a** is indicated by the *red dashed line*

good, moderate or poor skill in representing BSISO northward propagation. The meridional-vertical structure of U-wind, vorticity, pressure vertical velocity (W-wind), temperature (T), specific humidity (q), and total diabatic heating (Q) associated with intraseasonal convection over the Indian Ocean in each model was constructed based on regression analysis. The regression was performed using anomalous 3-D fields (only the climatological annual cycle was removed) against the 20–90 day band-pass-filtered rainfall averaged over the near equatorial box (85°–90°E; 5°–10°N). To focus more on the vertical structure rather than the amplitude, the regression coefficients were normalized for a constant 3 mm day^{-1} rainfall for all models. The observational counterparts were also computed using ERA-interim analysis and TRMM rainfall. The total diabatic heating based on ERA-interim was derived using the residual budget analysis approach (Yanai et al. 1973; Jiang et al. 2009). Composite meridional-vertical profiles of the six fields averaged over 80°–100°E are shown in Fig. 12 for models having good, moderate and poor skill in representing BSISO northward propagation. Composites were constructed using nine models in each category.

The vertical structure of BSISO in reanalysis is consistent with other previous studies (Jiang et al. 2004, 2011; Halder et al. 2012). Northward propagation of BSISO is known to be associated with barotropic vorticity and planetary boundary layer (PBL) moisture convergence leading the convection (Jiang et al. 2004). Positive vorticity is to the north of convection center with westerlies to the south and easterlies to the north. The equivalent barotropic structure in U wind and vorticity anomalies is evident in reanalysis and the good GCMs composite. In poor GCMs, the zonal wind and vorticity anomalies are restricted to the lower troposphere and the equivalent barotropic structure is not clear. The moderate GCM composite shows a mixed character—the equivalent barotropic structure is present but the lower level winds are more stronger that the upper level winds. In reanalysis the maximum vertical velocity (w-wind) appears in the mid-troposphere (around 400–500 hPa) coinciding with the convection center and a clear southward tilt with height is observed in the W wind and Q fields. This tilt is not very clear in the moderate and poor GCMs composite and also the region of upward vertical motion and positive diabatic heating is more latitudinally restricted. Differences are also evident in the temperature field, the second baroclinic mode vertical structure of T with positive anomalies in upper troposphere, is not captured faithfully in the poor GCMs. For the good and moderate models the second baroclinic mode of T appears more vertically stretched out compared to reanalysis. While these composites reflect the differences in vertical structures of dynamic and thermodynamic fields, the relationship between the models fidelity in simulating the northward propagation and the accurate representation of vertical profiles is explored in Fig. 13, across all 27 models. The individual models' meridional-vertical profiles for the aforesaid fields where compared with the observed profiles from ERA-interim and the pattern correlation skill scores were obtained. The results are displayed in Fig. 13 along with the BSISO northward propagation skill scores. Red and blue dots represent models that have good versus poor northward propagation characteristics respectively. A high correlation is observed for all the fields, especially u, vorticity, w and Q, indicating that realistic representation of vertical structures in these dynamical and thermo-dynamical fields has a critical role in a model's ability to simulate BSISO northward propagation.

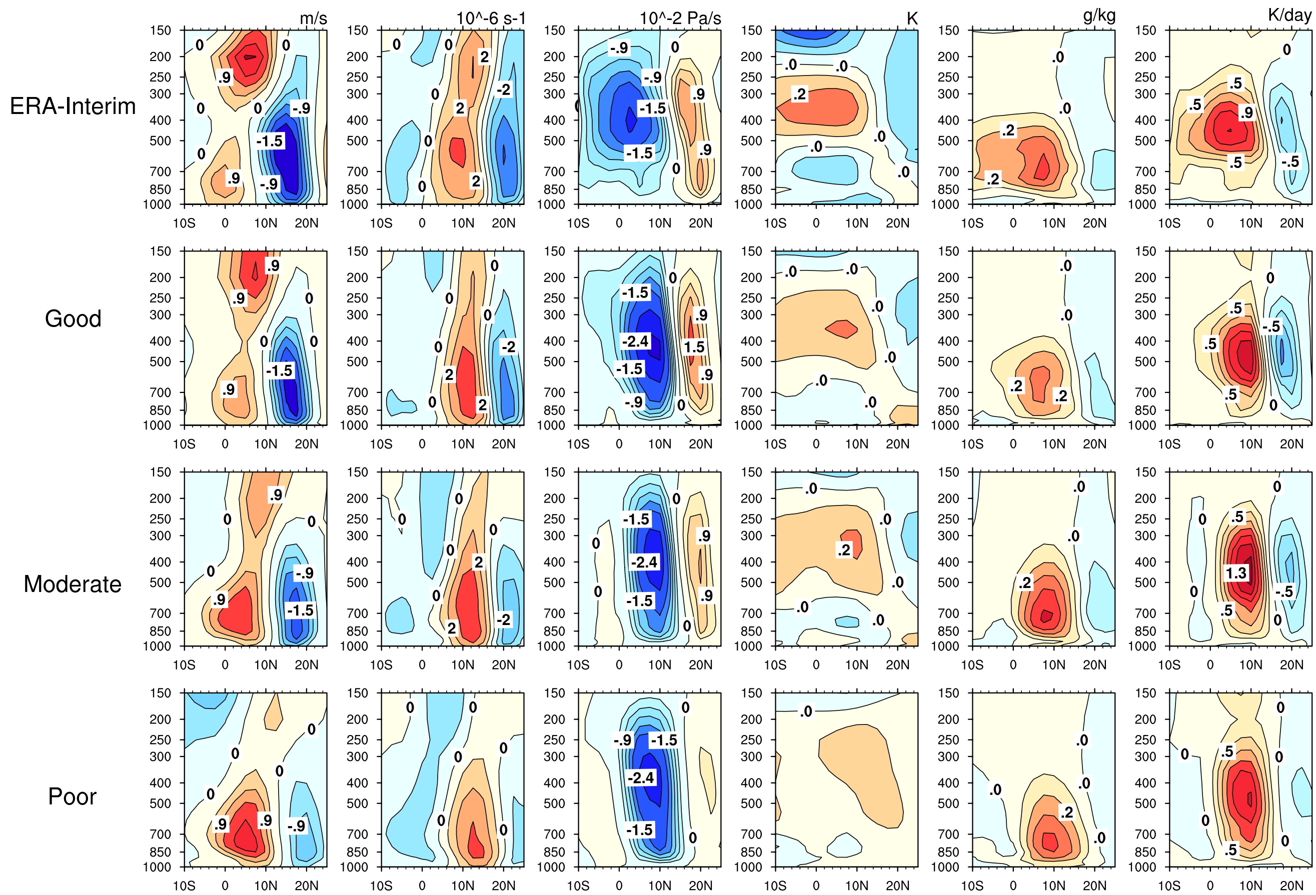

Fig. 12 Meridional-vertical profiles of lag-zero regressed anomalies of zonal wind. **a** (U-wind), **b** vorticity, **c** vertical velocity (W-wind), **d** temperature (T), **e** specific humidity (q) and **f** total diabatic heating (Q). The anomalous fields were regressed w.r.t 20–90 day band-pass-filtered rainfall area averaged over (85°–90°E; 5°–10°N) based on (*top row*) ERA-interim, composites for GCMs with good (*second row*), moderate (*third row*) and poor (*bottom row*) representation of BSISO northward propagation. All variables are averaged over 80°–100°E

3.8 Process-oriented diagnostic metrics

3.8.1 Vertical shear of zonal and meridional wind

Theoretical considerations of northward propagation suggest that the easterly vertical shear of the summer mean monsoon flow may play a critical role in generating the barotropic vorticity to the north of convection, which leads to PBL convergence, facilitating northward propagation of BSISO (Jiang et al. 2004; Drbohlav and Wang 2005). The summer mean wind structure over the monsoon region is characterized by westerlies in the lower troposphere and strong easterlies in the upper troposphere, giving rise to strong easterly vertical shear (Fig. 14a). The association between the amplitude of seasonal mean vertical wind shear (U200-U850) and the model fidelity in simulating northward propagation of BSISO across 27 GCM simulations is examined in Fig. 14c. The amplitude of vertical shear is obtained by averaging the vertical shear of zonal wind over the domain 0°–15°N, 70°–95°E. The vertical shear amplitude in reanalyses is −18.2 m/s. Overall there is no significant relationship between the model vertical shear strength and skill for northward propagation ($r = 0.11$). One notable model is PNU-CFS, which is one of the best models for BSISO northward propagation, but does a poor job in simulating the upper-level easterlies and easterly vertical shear.

Another theory on BSISO northward propagation, put forth by Bellon and Sobel (2008b) based on an intermediate aquaplanet model indicates that the barotropic vorticity to the north of BSISO convection is generated through meridional advection of baroclinic vorticity anomalies by the mean meridional wind shear. The summer mean meridional wind structure over the monsoon region is characterized by low-level southerlies associated with the cross-equatorial flow and northerly wind shear is observed close to the equator (Fig. 14b). The association between the amplitude of seasonal mean vertical shear of meridional wind

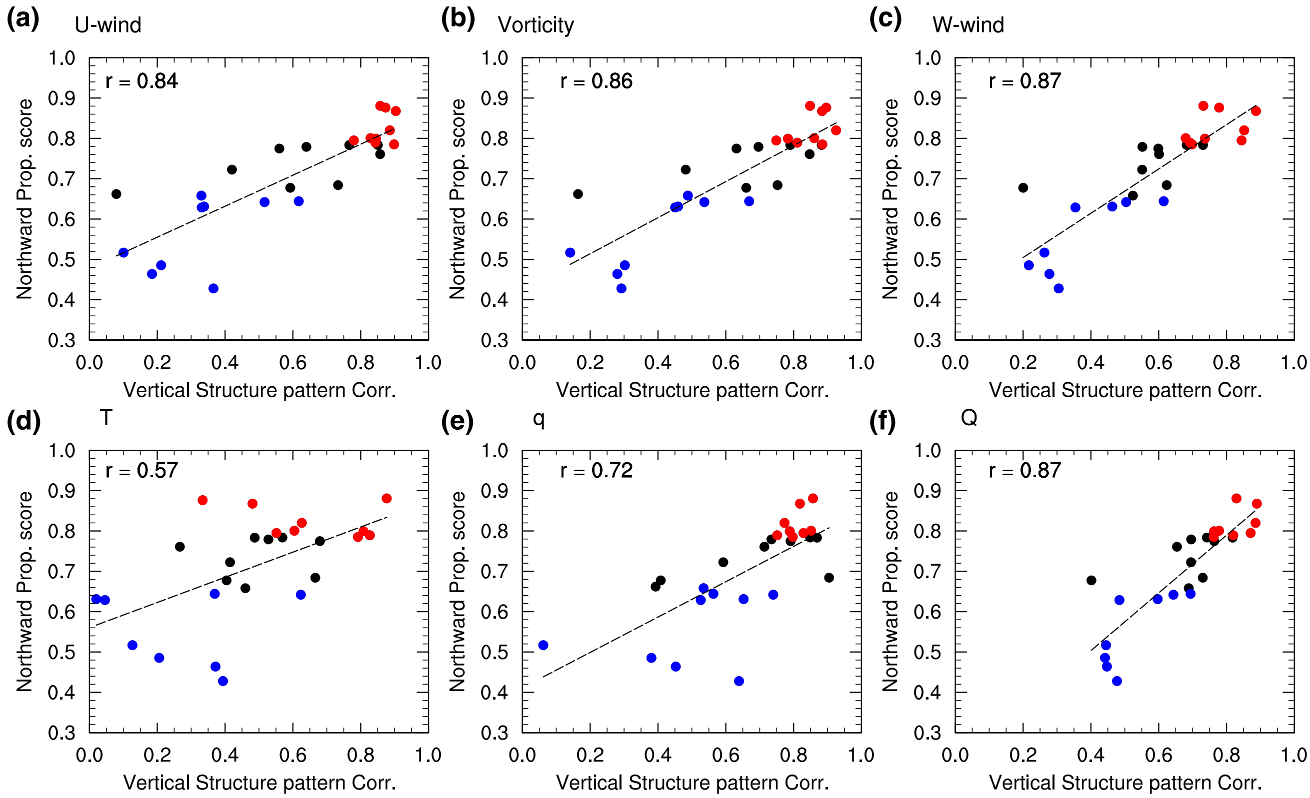

Fig. 13 Pattern correlations for the meridional-vertical profiles of **a** (U-wind), **b** Vorticity, **c** vertical velocity (W-wind), **d** temperature (T), **e** specific humidity (q) and **f** total diabatic heating (Q), in the 27 GCMs shown against the respective skill scores for BSISO northward propagation. *Red* and *blue dots* represent models with good versus poor skill for BSISO northward propagation. Correlations and least squares fit lines are also shown in each *panel*

(V200–V850) and the model fidelity in simulating northward propagation of BSISO across 27 GCM simulations is examined in Fig. 14d. The amplitude of vertical shear is calculated over the domain 0°–15°N, 70°–95°E. The vertical shear amplitude in reanalysis is −3.7 ms^{-1} (indicated by the dashed line). Overall there is no significant relationship between the meridional wind shear strength and skill for northward propagation (r = 0.31). These results suggest that the strength of mean zonal and meridional easterly vertical wind shear and vertical shear of meridional may not have a decisive role in controlling BSISO northward propagation, and hence indicates that other driving factors need to be identified.

3.8.2 Large-scale and convective rainfall partitioning

During boreal summer over the monsoon domain, about 20–40 % of the total rainfall is of stratiform origin (Schumacher and Houze 2003). Chattopadhyay et al. (2009) showed that the northward propagating BSISO is largely dominated by the stratiform component. The top heavy heating structure observed in the BSISO vertical profiles (Fig. 12) also suggests the role of stratiform heating (Houze 1982). Hence, getting the partitioning between convective and stratiform precipitation correctly is expected to impact the diabatic heating structure and hence the northward propagation. In GCM simulations the large-scale precipitation output is often treated analogous to stratiform precipitation, even though the two quantities are definitely not directly comparable (Seo and Wang 2010). The large-scale rain fraction in summer mean rainfall over the Indian Ocean box (60°–100°E, 10°S–15°N) is shown in Fig. 15. GISS-E2, GEOS5 and MRI-AGCM3 show relatively large values for large-scale rain fraction compared to the other models (0.6, 0.4 and 0.32 respectively). But, no significant correlation was observed between the magnitude of seasonal mean large-scale rain fraction and BSISO northward propagation skill score (r = 0.18, not shown). Figure 16 illustrates total, convective and large-scale rainfall anomalies associated with the northward propagation of BSISO in five models with highest skill scores for BSISO northward propagation (large-scale rain data is not available from PNU-CFS and SPCCSM3). The northward propagation of BSISO has a stronger contribution from the convective rainfall in ECHAM6 and ECEarth3; but for ECHAM5-SIT, GOES5, and GISS-E2, large-scale rainfall contribution is

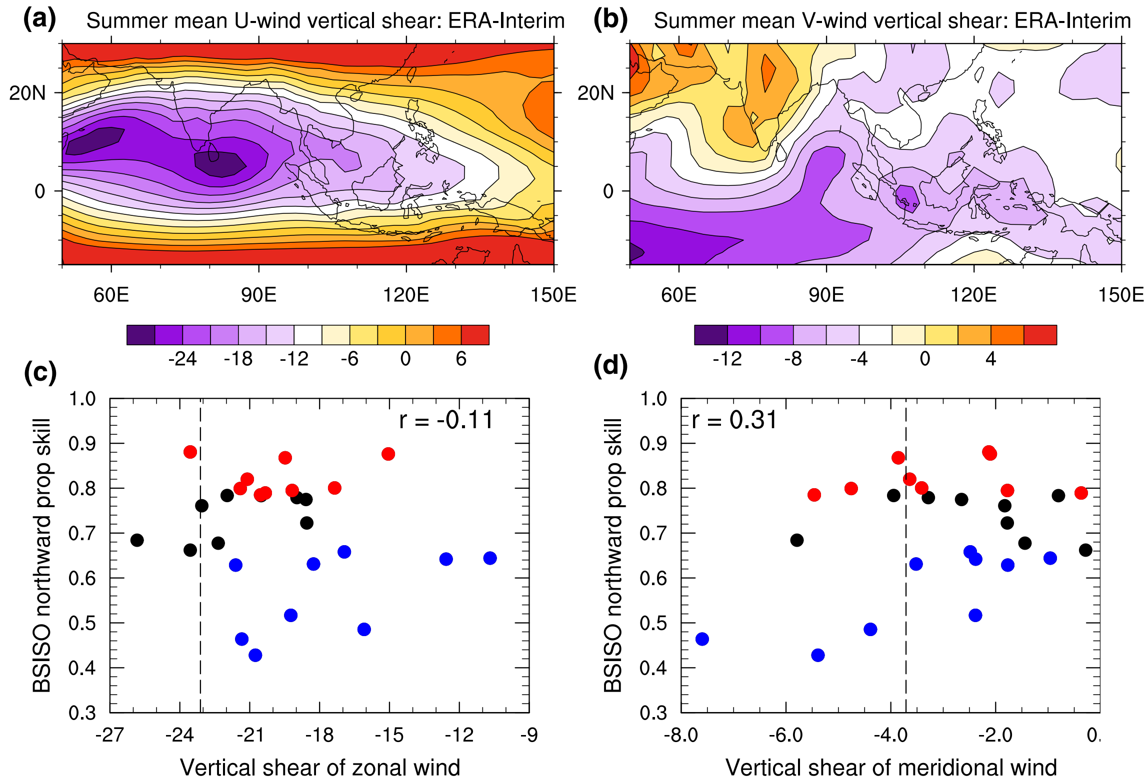

Fig. 14 **a** Summer mean vertical shear of zonal wind (U200-U850 hPa) and **b** Summer mean vertical shear of meridional wind (V200–V850 hPa) based on ERA-interim reanalysis. Average vertical shear of **c** zonal wind and **d** meridional wind over the domain 70°–95°E and 0°–15°N in the 27 GCM simulations, plotted against the corresponding BSISO northward propagation skill scores. The *dashed line* represents the average vertical shear (m s^{-1}) in ERA-interim reanalysis

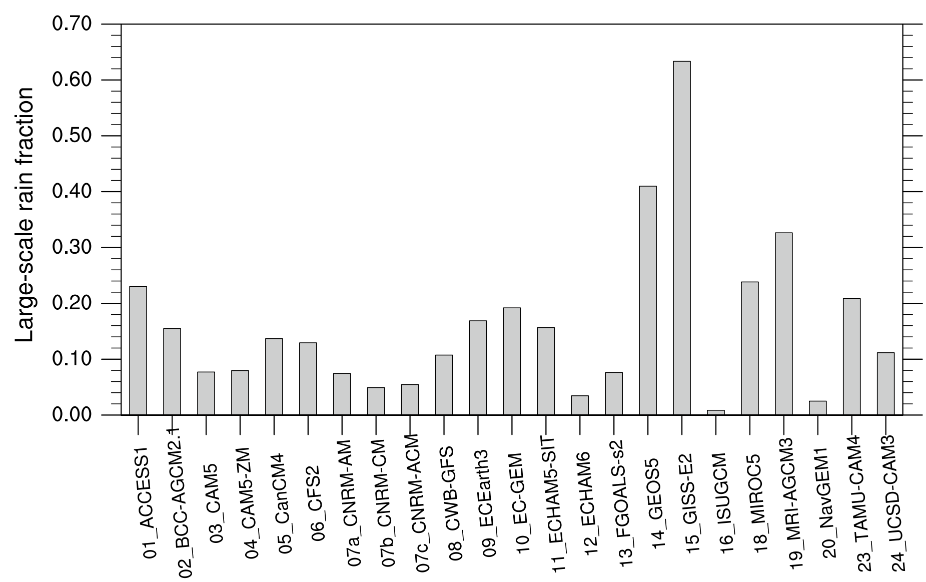

Fig. 15 Summer mean large-scale rainfall as a fraction of total rainfall averaged over the domain 60°–120°E, 10°S–15°N

comparable to the convective component. Hence we cannot draw a conclusive argument as to the role of convective versus large-scale rainfall partitioning in BSISO northward propagation.

3.8.3 Convection-moisture sensitivity

The observed relationship between atmospheric column moistening and convection found in both observations and

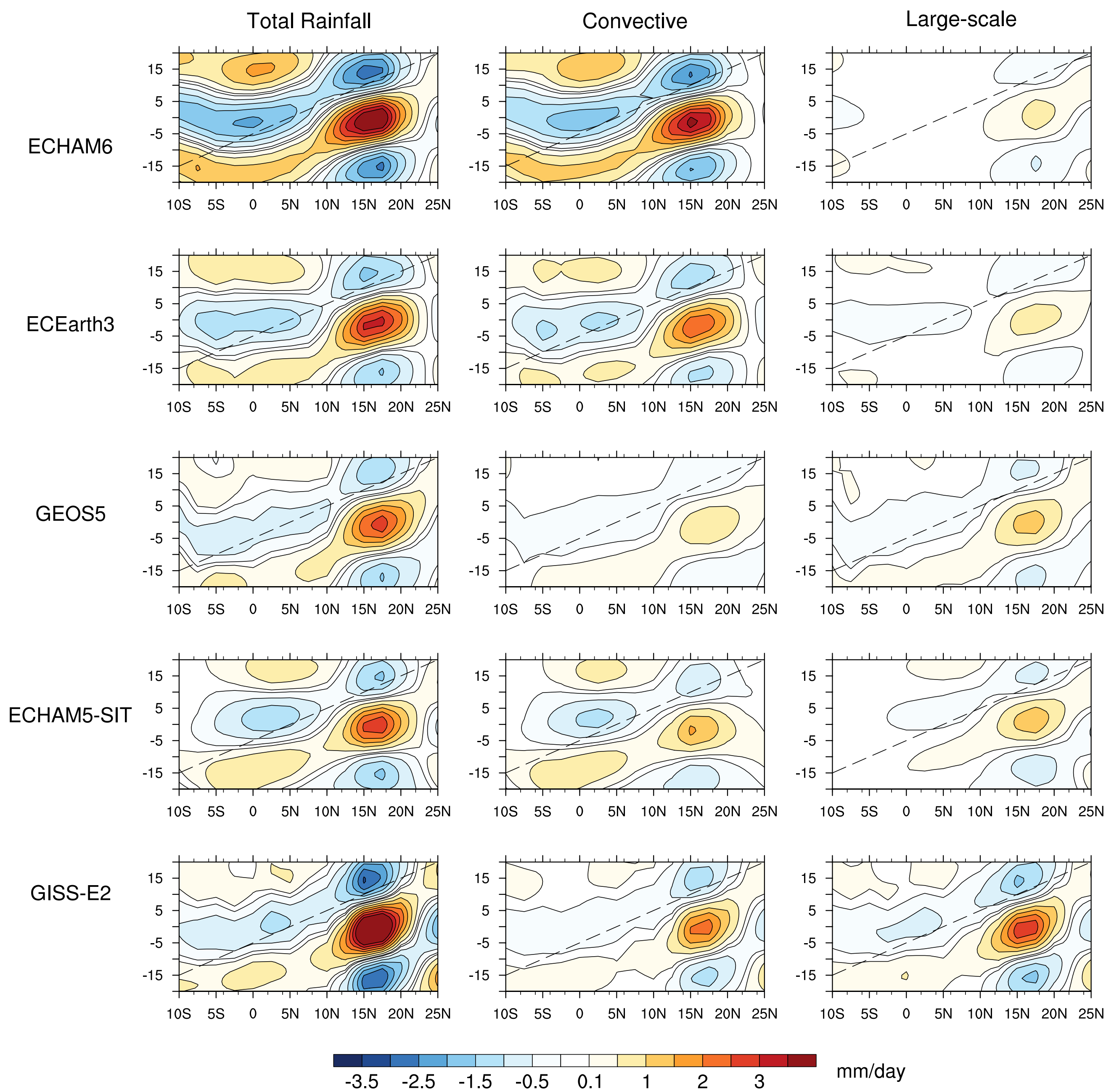

Fig. 16 BSISO northward propagation in total (*left column*), convective (*middle column*) and large-scale (*right column*) rainfall anomalies in five models with largest skill scores for northward propagation. Regression region is same as in Fig. 5 (Unit: mm day $^{-1}$)

model simulations (Bretherton et al. 2004; Holloway and Neelin 2009) has led to the development of relative humidity (RH) based diagnostic metrics (Raymond 2001; Thayer-Calder and Randall 2009; Sobel and Maloney 2012), which have been proven to be useful for assessing the skill of winter MJO (Kim et al. 2014; Jiang et al. 2015) and also for the eastern Pacific intraseasonal variability (Maloney et al. 2014). These RH diagnostic metrics are designed to measure the convection-moisture sensitivity in GCMs, e.g., the difference in lower tropospheric moisture between heavy and light rain events. In the following, we also test this RH diagnostic for the BSISO northward propagation skill.

Following previous studies, vertical profiles of RH at every grid point in the domain 60°–100°E and 10°S–15°N, were composited as a function of daily precipitation amplitude (mm day^{-1}). Fifty-one precipitation bins were used for compositing following Kim et al. (2014). The zero precipitation days were also included. Figure 17a shows the composite of ERA-interim RH as a function of TRMM precipitation amplitude. The X-axis is represented in a logarithmic

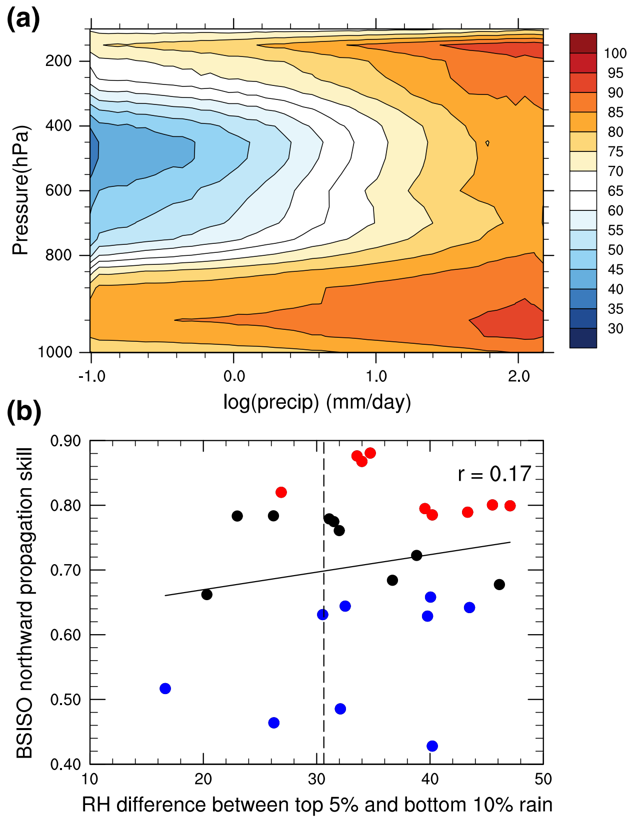

Fig. 17 **a** Composite vertical structure of relative humidity (RH) in the domain (60°–100°E; 10°S–15°N), in ERA-Interim reanalysis as a function of TRMM daily precipitation. **b** BSISO northward propagation skill scores plotted against the RH metric 850–500 hPa mass-weighted RH difference between the *top* 5 % and *bottom* 10 % of daily rainfall values. *Red* and *blue dots* represent models with good versus poor skill for BSISO northward propagation. The *dashed vertical line* gives the observed RH metric value

scale. Similar composites were generated based on model simulations. To account for the differences in precipitation intensity in different models, rather than choosing a fixed threshold for defining heavy and light rain events, precipitation percentiles were used. Through several sensitivity tests, the RH diagnostic was computed as the difference in the vertically averaged lower-tropospheric (850–500 hPa, mass-weighted) RH between the 95th and 10th ‰ of precipitation. Figure 17b shows the RH diagnostic for different models versus the models' skill for BSISO northward propagation. Only a weak 0.17 correlation is observed, implying the RH diagnostic may not be a useful diagnostic for BSISO northward propagation.

4 Summary and conclusions

Multi-model evaluation of BSISO is carried out in the 20-year climate simulations from 27 GCMs, as part of the year of tropical convection (YOTC) MJO task force (MJOTF) and GEWEX global atmospheric system study (GASS) program. A set of evaluation metrics were developed and used to assess the simulations of summer mean state, intraseasonal variance, horizontally tilted structure of convective rain-band, vertical structure of BSISO, and dominant propagation characteristics of BSISO, including equatorial eastward propagation, northward propagation in the Asian monsoon domain, and westward propagation from western Pacific to Indian Ocean associated with the quasi-biweekly mode. The validity of some reported relationships were also tested, such as, the relationship between model skill for simulating summer mean and ISV, eastward and northward propagation of BSISO, and vertical mean wind shear and northward propagation. Process diagnostics based on convective versus large-scale rainfall partitioning and relative humidity diagnostics were applied to model simulations to test their usability with respect to BSISO northward propagation.

Large biases are observed in the models' depiction of summer mean (May–October) state (Fig. 1). Underestimation of mean rainfall over land (e.g. Indian land region), overestimation of precipitation over the western–north Pacific and other warm SST regions are some notable biases. Intraseasonal variance bears a very similar spatial pattern as the seasonal mean. But, the amplitude of BSISO is largely underestimated in at least two-thirds of the models, more so over the convective hotspots over the Indian Ocean and Bay of Bengal (Fig. 2). Multi-model mean bias is largely negative over IO and WP in both the summer mean and intraseasonal variance representation, and the western EQIO, BoB and WNP are regions with generally large RMSE (Fig. 3). The stationary BSISO variance structure was also found to be a good indicator to how well the models simulate the propagating mode. Consistent with Sperber et al. (2013), BSISO life cycle skill scores brought out by EEOF based composites, were found to be in good agreement with how well the BSISO variance pattern is simulated (Fig. 4).

Lag regression analysis was used to evaluate the propagation features of BSISO. Large discrepancies were observed in the model depiction of the northward propagating mode. Even in models that show some fidelity in simulating the northward propagation, often the phase speed and meridional extent of the mode is misrepresented (Fig. 6). A good association is evident between the simulation of eastward and northward propagation of BSISO, in many models, indicating that in general GCMs are successful in simulating the observed link between these propagating modes (Fig. 8b). Nevertheless model fidelity in simulating the eastward propagation is not a mandatory condition for a realistic simulation of the northward propagation, as evidenced by a group of GCMs. Moreover, a good association is found between the summertime MJO eastward propagation skill and the earlier reported wintertime skill scores, indicating that models that are skillful in simulating the winter MJO generally also have similar skill during summer season (Fig. 8a). Since the main focus of the study is on BSISO northward propagation, other metrics and process diagnostics were tested with respect to the BSISO northward propagation skill scores.

Simulating the northwest–southeastward (NW–SE) tilted rain band of BSISO still remains a challenge for the GCMs (e.g. Waliser et al. 2003; Sperber and Annamalai 2008; Sabeerali et al. 2013). A quantitative estimate of the simulated tilt of the convective rain-band was made (Figs. 10, 11). All the models underestimate the tilt and this is noted as a systematic bias in the models bearing a good association with the model's ability in simulating BSISO northward propagation ($r = 0.52$). In at least 2/3rd of the models, the northwest–southeast tilted structure is absent. The importance of simulating the seasonal mean vertical shear of zonal as well as meridional wind was also examined for being a requisite condition for BSISO northward propagation. BSISO northward propagation skill scores do not show any significant relationship with the seasonal mean vertical shear of either zonal wind or meridional wind over the Indian Ocean domain (Fig. 14). Vertical profiles of dynamic and thermodynamic fields (zonal wind, vorticity, vertical velocity, specific humidity, temperature and total diabatic heating) associated with BSISO convection were generated for models with good, moderate and poor representation of BSISO northward propagation (Fig. 12). Notable differences were observed in the composite fields for these categories. The simulation of equivalent barotropic vorticity north of convection is shallow and of a smaller meridional scale in the models with poor northward propagation skill. They also have difficulty in simulating the second baroclinic vertical mode in temperature anomalies. The southward tilt with height observed in the vertical profiles of temperature and diabatic heating is stronger in the GCMs with good northward propagation representation. Moreover, simulations of vertical profiles are found to be strongly linked to the northward propagation of BSISO, with strong pattern correlations existing between vertical-latitudinal profiles of different fields and the northward propagation skill scores (Fig. 13).

Earlier studies indicate that the stratiform rainfall and associated top-heavy heating play a major role in BSISO northward propagation (Chattopadhyaya et al. 2009). The convective versus large scale rainfall partitioning in the model simulations were examined along with model skill for BSISO northward propagation. However, a clear relationship is not evident between large-scale rainfall partitioning and northward propagation skill (Figs. 15, 16). The relative humidity diagnostic, which was shown to be a useful metric for MJO, was also tested for its usability as a diagnostic for BSISO northward propagation. Vertical composite profiles of RH were generated for the Indian Ocean domain as a function of daily precipitation amplitude, to assess the convection-moisture sensitivity and its relation to northward propagation. Lower tropospheric (850–500 hPa) RH composite difference for bottom 10 % and top 5 % of rainfall cases, showed a large spread in the GCM simulations and it was not related to model skill for the BSISO northward propagation skill of the models (Fig. 17). This is in contrast to the statistically significant relationship observed between the RH-precipitation metric and winter MJO fidelity in Jiang et al. (2015). This difference may be attributed either to the difference in the boreal summer and boreal-winter mean state, or the fundamental differences between MJO and BSISO. It may also be indicative that the metric design does not fully take into account the processes important for simulating BSISO. Another notable difference in MJO and BSISO fidelity is related to the importance of air–sea coupling. Based on the CNRM model simulations, Jiang et al. (2015) illustrated that air–sea interaction could be important for realistic simulation of the MJO in this model. The eastward propagation of MJO was better simulated in the coupled model (CNRM-CM) compared to the AGCM run (CNRM-AM). But such improvement in simulations of BSISO northward propagation by considering the air–sea coupling is not clearly evident in CNRM-CM run (Fig. 6). Combining the understanding based on these two studies, it may be inferred that there exists certain seasonal variations in the mean-state biases in the coupled GCM simulations and which impacts the model skill in representing intraseasonal modes during different seasons.

Evaluation of BSISO in the 27 GCM simulations show that the representation of some BSISO features in the new generation GCMs (e.g. YOTC/MJOTF-GASS study) are better than the older generation GCMs (Kang et al. 2002; Waliser et al. 2003; Lin et al. 2008). Although significant biases are seen in summer mean precipitation simulations, simulations of wind fields are improved, and at least in some GCMs the northward propagation is very close to observations. Many models are successful in simulating the eastward propagation associated with northward propagation. Long-standing problems persist, such as simulating the tilted rain-band structure associated with BSISO. Vertical wind shear, RH diagnostic, and large-scale rain fraction do not show a direct relationship with the northward propagation skill in GCMs. More focused process-oriented diagnostic metrics need to be developed for the northward propagating component of BSISO.

Acknowledgments The multi-model output analyzed in this study is available for free download from https://earthsystemcog.org/projects/gassyotc-mip/. This study was supported by Indian National Monsoon Mission. Neena Mani and Xianan Jiang acknowledge the support of JIFRESSE-UCLA. X. Jiang acknowledges support by US NSF Climate and Large-Scale Dynamics Program under Award AGS-1228302, and NOAA Climate Program Office under Awards NA12OAR4310075, NA15OAR4310098, and NA15OAR4310177. D. W.'s contribution was carried out on behalf of the Jet Propulsion Laboratory, California Institute of Technology, under a contract with NASA. We thank Drs. Ken Sperber, Harry Hendon and Steve Woolnough for useful suggestions and discussions that helped this study.

References

Abhilash S, Sahai AK, Pattanaik S, Goswami BN, Kumar A (2014) Extended range prediction of active-break spells of Indian summer monsoon rainfall using an ensemble prediction system in NCEP climate forecast system. Int J Climatol 34:98–113

Annamalai H, Slingo JM (2001) Active/break cycles: diagnosis of the intraseasonal variability of the Asian summer monsoon. Clim Dyn 18:85–102

Annamalai H, Sperber KR (2005) Regional heat sources and the active and break phases of boreal summer intraseasonal (30–50 day) variability. J Atmos Sci 62:2726–2748

Bechtold P, Kohler M, Jung T, Doblas-Reyes F, Leutbecher M, Rodwell MJ, Vitart F, Balsamo G (2008) Advances in simulating atmospheric variability with the ECMWF model: from synoptic to decadal time-scales. Q J Meteorol Soc 134:1337–1351

Bellon G, Sobel A (2008a) Poleward-propagating intraseasonal monsoon disturbances in an intermediate-complexity axisymmetric model. J Atmos Sci 65:470–489

Bellon G, Sobel A (2008b) Instability of the axisymmetric monsoon flow and intraseasonal oscillation. J Geophys Res 113:D07109. doi:10.1029/2007JD008968

Benedict JJ, Randall DA (2007) Observed characteristics of the MJO relative to maximum rainfall. J Atmos Sci 64:2332–2354

Bessafi M, Wheeler MC (2006) Modulation of south Indian ocean tropical cyclones by the Madden–Julian oscillation and convectively coupled equatorial waves. Mon Weather Rev 134:638–656

Bollasina M, Ming Y (2013) The general circulation model precipitation bias over the southwestern equatorial Indian Ocean and its implications for simulating the South Asian monsoon. Clim Dyn 40:823–838

Boos WR, Kuang Z (2010) Mechanisms of poleward propagating, intraseasonal convective anomalies in cloud system-resolving models. J Atmos Sci 67:3673–3691

Bretherton CS, Peters ME, Back LE (2004) Relationships between water vapor path and precipitation over the tropical oceans. J Clim 17:1517–1528

Chatterjee P, Goswami BN (2004) Structure, genesis and scale selection of the tropical quasi-biweekly mode. Q J R Meteorol Soc 130:1171–1194

Chattopadhyay R, Goswami BN, Sahai AK, Fraedrich (2009) Role of stratiform rainfall in modifying the northward propagation of monsoon intraseasonal oscillation. J Geophys Res 114:D19114

Dee DP et al (2011) The ERA-interim reanalysis: configuration and performance of the data assimilation system. Q J R Meteorol Soc 137:553–597

DeMott CA, Stan C, Randall DA (2013) Northward propagation mechanisms of the boreal summer intraseasonal oscillation in the ERA-interim and SP-CCSM. J Clim 26:1973–1992

Drbohlav H-K, Wang (2005) Mechanism of the northward-propagating intraseasonal oscillation: insights from a zonally symmetric model. J Climate 20:952–972

Fu X, Wang B, Li T, McCreary JP (2003) Coupling between northward-propagating, intraseasonal oscillations and sea surface temperature in the Indian Ocean. J Atmos Sci 60:1733–1753

Gleckler PJ, Taylor KE, Doutriaux C (2008) Performance metrics for climate models. J Geophys Res Atmos 113:D06104

Goswami BN (2005) South Asian monsoon, Chapter 2. In: Lau WKM, Waliser DE (eds) Intraseasonal variability of the atmosphere-ocean climate system. Praxis, Springer, Berlin, pp 19–61

Goswami BN, Ajaya Mohan RS (2001) Intra-seasonal oscillations and inter-annual variability of the Indian summer monsoon. J Clim 14:1180–1198

Goswami BN, Ajaya Mohan RS, Xavier PK, Sengupta D (2003) Clustering of synoptic activity by Indian summer monsoon intraseasonal oscillations. Geophys Res Lett 30(8):1431

Halder M, Mukhopadhyay P, Halder S (2012) Study of the microphysical properties associated with the monsoon intraseasonal oscillation as seen from the TRMM observations. Ann Geophys 30:897–910

Hendon HH, Liebmann B (1990) The intraseasonal (30–50 day) oscillation of the Australian summer monsoon. J Atmos Sci 47:2909–2924

Holloway CE, Neelin JD (2009) Moisture vertical structure, column water vapor, and tropical deep convection. J Atmos Sci 66:1665–1683

Houze RA (1982) Cloud clusters and large-scale vertical motions in the tropics. J Meteor Soc Jpn 60:396–410

Huffman GJ, Adler RF, Rudolf B, Schneider U, Keehn PR (1995) Global precipitation estimates based on a technique for combining satellite-based estimates, rain-gauge analysis, and NWP model precipitation information. J Clim 8:1284–1295

Jiang X, Waliser DE (2008) Northward propagation of the subseasonal variability over the eastern Pacific warm pool. Geophys Res Lett 35:L09814

Jiang X, Waliser DE (2009) Two dominant subseasonal variability modes of the eastern Pacific ITCZ. Geophys Res Lett 36:L04704

Jiang X, Li T, Wang B (2004) Structures and mechanisms of the northward propagating boreal summer intraseasonal oscillation. J Clim 17:1022–1039

Jiang X et al (2009) Vertical heating structures associated with the MJO as characterized by TRMM estimates, ECMWF reanalyses, and forecasts: a case study during 1998/99 winter. J Clim 22:6001–6020

Jiang X, Waliser DE, Li J-L, Woods C (2011) Vertical cloud structures of the boreal summer intraseasonal variability based on CloudSat observations and ERA-interim reanalysis. Clim Dyn 36:2219–2232

Jiang X et al (2015) Vertical structure and physical processes of the Madden–Julian oscillation: exploring key model physics in climate simulations. J Geophys Res Atmos 120:4718–4748

Kang I-S et al (2002) Intercomparison of the climatological variations of Asian summer monsoon precipitation simulated by 10 GCMs. Clim Dyn 19:383–395

Kang I-S, Kim D, Kug J-S (2010) Mechanism for northward propagation of boreal summer intraseasonal oscillation: convective momentum transport. Geophys Res Lett 37: L24804

Kemball-Cook S, Wang B (2001) Equatorial waves and air–sea interaction in the boreal summer intraseasonal oscillation. J Clim 14:2923–2942

Khairoutdinov M, DeMott C, Randall D (2008) Evaluation of the simulated interannual and subseasonal variability in an AMIP-style simulation using the CSU multiscale modeling framework. J Clim 21:413–431

Kikuchi K, Wang B (2009) Global perspective of the quasi-biweekly oscillation. J Clim 22:1340–1359
Kikuchi K, Wang B, Kajikawa Y (2011) Bimodal representation of the tropical intraseasonal oscillation. Clim Dyn. doi:10.1007/s00382-011-1159-1
Kim D, Sobel AH, Maloney ED, Frierson DMW, Kang I-S (2011) A systematic relationship between intraseasonal variability and mean state bias in AGCM simulations. J Clim 24:5506–5520
Kim D et al (2014) Process-oriented MJO simulation diagnostic: moisture sensitivity of simulated convection. J Clim 27:5379–5395
Klingaman NP, Woolnough SJ (2014) Using a case-study approach to improve the Madden–Julian oscillation in the Hadley Centre model. Q J R Meteorol Soc 140:2491–2505
Klingaman NP et al (2015a) Vertical structure and physical processes of the Madden–Julian oscillation: linking hindcast fidelity to simulated diabatic heating and moistening. J Geophys Res Atmos. doi:10.1002/2014JD022374
Klingaman NP, Jiang X, Xavier PK, Petch J, Waliser D, Woolnough SJ (2015b) Vertical structure and physical processes of the Madden–Julian oscillation: synthesis and summary. J Geophys Res Atmos. doi:10.1002/2015JD023196
Lappen C-L, Schumacher C (2012) Heating in the tropical atmosphere: what level of detail is critical for accurate MJO simulations in GCMs? Clim Dyn 39:2547–2568
Lau KM, Chan PH (1988) Intraseasonal and interannual variations of tropical convection: a possible link between the 40–50 day oscillation and ENSO? J Atmos Sci 45:506–521
Lau KM, Waliser DE (2011) Intraseasonal variability of the atmosphere-ocean climate system, 2nd edn. Springer, Heidelberg, p 613
Lawrence DM, Webster PJ (2002) The boreal summer intraseasonal oscillation: relationship between northward and eastward movement of convection. J Atmos Sci 59:1593–1606
Lin J-L et al (2006) Tropical intraseasonal variability in 14 IPCC AR4 climate models. Part I: convective signals. J Clim 19:2665–2690
Lin J-L et al (2008) Subseasonal variability associated with Asian summer monsoon simulated by 14 IPCC AR4 coupled GCMs. J Clim 21:4541–4567
Madden RA (1986) Seasonal-variations of the 40–50 day oscillation in the tropics. J Atmos Sci 43:3138–3158
Madden RA, Julian PR (1972) Description of global-scale circulation cells in tropics with a 40–50 day period. J Atmos Sci 29:1109–1123
Madden RA, Julian PR (1994) Observations of the 40–50-day tropical oscillation: a review. Mon Weather Rev 122:814–837
Maloney ED, Esbensen SK (2007) Satellite and buoy observations of boreal summer intraseasonal variability in the tropical northeast Pacific. Mon Weather Rev 135:3–19
Maloney ED, Hartmann DL (2001) The sensitivity of intraseasonal variability in the NCAR CCM3 to changes in convective parameterization. J Clim 14:2015–2034
Maloney ED, Jiang X, Xie S-P, Benedict J (2014) Process-oriented diagnosis of East Pacific warm pool intraseasonal variability. J Clim 27:6305–6324
McPhaden MJ (1999) Genesis and evolution of the 1997–98 El Nino. Science 283:950–954
Neena JM, Goswami BN (2010) Extension of potential predictability of Indian summer monsoon dry and wet spells in recent decades. Q J R Meteorol Soc 136:583–592
Oh JH, Kim KY, Lim GH (2012) Impact of MJO on the diurnal cycle of rainfall over the western Maritime Continent in the austral summer. Clim Dyn 38:1167–1180
Petch J, Waliser D, Jiang X, Xavier P, Woolnough S (2011) A global model inter-comparison of the physical processes associated with the MJO. GEWEX News 21(3):3–5
Phillips TJ, Potter GL, Williamson DL, Cederwall RT, Boyle JS, Fiorino M, Hnilo JJ, Olson JG, Xie S, Yio JJ (2004) Evaluating parameterizations in general circulation models: climate simulation meets weather prediction. Bull Am Meteorol Soc 85:1903–1915
Randall D, Khairoutdinov M, Arakawa A, Grabowski W (2003) Breaking the cloud parameterization deadlock. Bull Am Meteor Soc 84:1547–1564
Raymond DJ (2001) A new model of the Madden–Julian oscillation. J Atmos Sci 58:2807–2819
Reynolds RW, Rayner NA, Smith TM, Stokes DC, Wang W (2002) An improved in situ and satellite SST analysis for climate. J Clim 15:1609–1625
Sabeerali CT, Dandi AR, Dhakate A, Salunke K, Mahapatra S, Rao SA (2013) Simulations of boreal summer intraseasonal oscillations in the latest CMIP5 coupled GCMs. J Geophys Res Atmos 118:4401–4420
Schumacher C, Houze RA (2003) Stratiform rain in the tropics as seen by the TRMM precipitation radar. J Clim 16:1739–1756
Seo KH, Wang WQ (2010) The Madden–Julian oscillation simulated in the NCEP climate forecast system model: the importance of stratiform heating. J Clim 23:4770–4793
Sikka DR, Gadgil S (1980) On the maximum cloud zone and the ITCZ over Indian longitudes during the southwest monsoon. Mon Weather Rev 108:1840–1853
Sobel A, Maloney E (2012) An idealized semi-empirical framework for modeling the Madden–Julian oscillation. J Atmos Sci 69:1691–1705
Sperber KR, Annamalai H (2008) Coupled model simulations of boreal summer intraseasonal (30–50 day) variability, Part I: systematic errors and caution on use of metrics. Clim Dyn 31:345–372
Sperber KR et al (2000) Predictability and the relationship between subseasonal and interannual variability during the Asian summer monsoon. Q J Roy Meteorol Soc 126:2545–2574
Sperber KR et al (2001) Dynamical seasonal predictability of the Asian summer monsoon. Mon Weather Rev 129:2226–2248
Sperber KR, Annamali H, Kang I-S, Kitoh A, Moise A, Turner A, Wang B, Zhou T (2013) The Asian summer monsoon: an intercomparison of CMIP5 versus CMIP3 of the late twentieth-century. Clim Dyn 41:2711–2744
Stan C, Khairoutdinov M, DeMott CA, Krishnamurthy V, Straus DM, Randall DA, Kinter JL, Shukla J (2010) An ocean-atmosphere climate simulation with an embedded cloud resolving model. Geophys Res Lett 37(1):L01702. doi:10.1029/2009GL040822
Suhas E, Neena JM, Goswami BN (2013) An Indian monsoon intraseasonal ocsillations (MISO) index for real-time monitoring and forecast verification. Clim Dyn 40:2605–2616
Takayabu YN, Iguchi T, Kachi M, Shibata A, Kanzawa H (1999) Abrupt termination of the 1997–1998 El Nino in response to a Madden–Julian oscillation. Nature 402:279–282
Thayer-Calder K, Randall DA (2009) The role of convective moistening in the Madden–Julian oscillation. J Atmos Sci 66:3297–3312
Tian B, Waliser DE, Fetzer EJ (2006) Modulation of the diurnal cycle of tropical deep convective clouds by the MJO. Geophys Res Lett 33:L20704
Waliser DE (2006a) Intraseasonal variations. In: Wang B (ed) The Asian monsoon. Springer, Heidelberg, p 787
Waliser DE (2006b) Intraseasonal variability. In: Wang B (ed) The Asian monsoon. Springer, Heidelberg, p 844
Waliser DE, Stern W, Schubert S, Lau KM (2003a) Dynamic predictability of intraseasonal variability associated with the Asian summer monsoon. Q J R Meteorol Soc 129:2897–2925
Waliser DE, Jin K, Kang IS, Stern WF, Schubert SD, Wu MLC, Lau KM, Lee MI, Krishnamurthy V, Kitoh A, Meehl GA, Galin VY, Satyan V, Mandke SK, Wu G, Liu Y, Park CK (2003b) AGCM

simulations of intraseasonal variability associated with the Asian summer monsoon. Clim Dyn 21(5–6):423–446
Waliser D, Sperber K, Hendon H, Kim D, Wheeler M, Weickmann K, Zhang C, Donner L, Gottschalck J, Higgins W, Kang IS, Legler D, Moncrieff M, Vitart F, Wang B, Wang W, Woolnough S, Maloney E, Schubert S, Stern W (2009) MJO simulation diagnostics. J Clim 22:3006–3030
Wang WQ, Schlesinger ME (1999) The dependence on convection parameterization of the tropical intraseasonal oscillation simulated by the UIUC 11-layer atmospheric GCM. J Clim 12:1423–1457
Wang B, Xie X (1997) A model for boreal summer intraseasonal oscillation. J Atmos Sci 54:72–86
Wang B, Webster P, Kikuchi K, Yasunari T, Qi YJ (2006) Boreal summer quasi-monthly oscillation in the global tropics. Clim Dyn 27:661–675
Webster PJ, Magana VO, Palmer TN, Shukla J, Tomas RA, Yanai M, Yasunari T (1998) Monsoons: processes, predictability, and the prospects for prediction. J Geophys Res 103:14451–14510
Wheeler M, Kiladis GN (1999) Convectively coupled equatorial waves: analysis of clouds and temperature in the wavenumber-frequency domain. J Atmos Sci 56:374–399
Xavier PK et al (2015) Vertical structure and physical processes of the Madden–Julian oscillation: biases and uncertainties at short range. J Geophys Res Atmos. doi:10.1002/2014JD022718
Yanai M, Esbensen S, Chu J-H (1973) Determination of bulk properties of tropical cloud clusters from large-scale heat and moisture budgets. J Atmos Sci 30:611–627
Zhang CD (2005) The Madden–Julian oscillation. Rev Geophys. doi:10.1029/2004RG000158
Zhang CD, Dong M (2004) Seasonality in the Madden–Julian oscillation. J Clim 17:3169–3180
Zhang GJ, Song X (2009) Interaction of deep and shallow convection is key to Madden–Julian oscillation simulation. Geophys Res Lett 36:L09708. doi:10.1029/2009GL037340
Zhou L, Neale RB, Jochum M, Murtugudde R (2012) Improved Madden–Julian oscillations with improved physics: the impact of modified convection parameterizations. J Clim 25:1116–1136